Electromagnetic Modeling within a Microscopically Realistic Brain – Implications for Brain Stimulation

Zhen Qi[1], Gregory M. Noetscher*[1], Alton Miles[1], Konstantin Weise[2,3], Thomas R. Knösche[2], Cameron R. Cadman[1], Alina R. Potashinsky[1], Kelu Liu[1], William A. Wartman[1], Guillermo Nunez Ponasso[1], Marom Bikson[4], Hanbing Lu[5], Zhi-De Deng[6], Aapo R. Nummenmaa[7], Sergey N. Makaroff[1]

(1) Department of Electrical and Computer Eng., Worcester Polytechnic Inst., Worcester MA USA

(2) Max Planck Inst. for Human Cognitive and Brain Sciences, Leipzig, Germany

(3) Leipzig University of Applied Sciences (HTWK), Faculty of Engineering, Leipzig, Germany

(4) Department of Biomedical Engineering, The City College of New York, New York NY USA

(5) Neuroimaging Research Branch, National Institute on Drug Abuse, Intramural Research Program, National Institutes of Health, Baltimore MD USA

(6) Computational Neurostimulation Research Program, Noninvasive Neuromodulation Unit, Experimental Therapeutics and Pathophysiology Branch, National Institute of Mental Health, National Institutes of Health, Bethesda MD USA

(7) Athinoula A. Martinos Ctr. for Biomedical Imaging, Massachusetts General Hospital, Charlestown MA USA

Abstract

Across all electrical stimulation (neuromodulation) domains, conventional analysis of cell polarization involves two discrete steps: i) prediction of macroscopic electric field, ignoring presence of cells and; ii) prediction of cell polarization from tissue electric fields. The first step assumes that electric current flow is not distorted by the dense tortuous network of cell structures. The deficiencies of this assumption have long been recognized, but – except for trivial geometries – ignored, because it presented intractable computation hurdles.

We leverage: i) recent electron microscopic images of the brain that have made it possible to reconstruct microscopic brain networks over relatively large volumes and; ii) a charge-based formulation of boundary element fast multipole method (BEM-FMM) to produce the first multiscale stimulations of realistic neuronal polarization by electrical stimulation that consider current flow distortions by a microstructure. The dataset under study is a 250×140×90 μm section of the L2/L3 mouse visual cortex with 396 tightly spaced neurite cells and 34 microcapillaries. We quantify how brain microstructure significantly distorts the primary macroscopic electric field. Although being very local, such distortions constructively accumulate along the neuronal arbor and reduce neuronal activating thresholds by 0.55-0.85-fold as compared to conventional theory.

Keywords:

Multiscale brain modeling
Boundary Element Fast Multipole Method (BEM-FMM)
Biophysical modeling
Brain stimulation

Data availability statement

Post-processed cell CAD models (383), microcapillary CAD models (34), post-processed neuron morphologies (267), extracellular field and potential distributions at different polarizations (267x3), *.ses projects files for biophysical modeling with Neuron software (267x2), and computed neuron activating thresholds at different conditions (267x8) are made available online through BossDB, a volumetric open-source database for 3D and 4D neuroscience data.

Significance statement

This study introduces a novel method for modeling perturbations of impressed electric fields within a microscopically realistic brain volume, including densely populated neuronal cells and blood microcapillaries. It addresses a limitation present across decades of macroscopic-level electromagnetic models for electrical stimulation. For the investigated brain volume, our model predicted a neural activation threshold reduction factor of 0.85–0.55 when compared to the macroscopic approach. The present study begins to bridge a long-recognized gap in our analysis of bioelectricity and provides a framework to evaluate (and compensate) for the adequacy of macroscopic models in brain stimulation and electrophysiology.

1. Introduction

Neuroscience and brain stimulation are rapidly advancing fields that rely on our ability to model electromagnetic fields within the brain. This modeling is essential for understanding the brain's intrinsic functions and its response to external stimuli, such as those provided by transcranial magnetic stimulation (TMS) [1], electrical stimulation (TES) [2], electroconvulsive therapy (ECT) [3], or similar excitation. However, accurately modeling these fields within the brain presents a great challenge due to the brain's complex microstructure, including the intricate networks of neurons and blood vessels [4],[5], all of which must be considered in the models.

While great insights have been established in the past ([6],[7],[8],[9],[10],[11]), the canonical approach of bioelectrical field modeling ignores all microscopic structures, with each region represented as macroscopically homogenous; neurons (and blood vessels) become "transparent" and do not exist in the physical sense of influencing current flow. Only after the macroscopic electric field is predicted are isolated neurons "reinserted" to model their response. Ignoring microstructure is a recognized limitation but treated as a *fait accompli* because of computational intractability, except for models of isolated and simplified neuronal and vascular geometries, where the importance is demonstrated [12]. The importance of realistic dense cell packing on electric fields (and resulting neuronal activation) cannot even be evaluated with the associated modeling tools based on the finite element method [13] – these are developed for the first time here.

For the present study, we target an exemplary subvolume of the L2/3 P36 mouse primary visual cortex [4],[5]. The high-resolution triangular surface meshes for cell membranes and blood vessel walls (~0.5 billion facets in total) are based on a semi-automated segmentation of scanning electron data [4],[5]. Conventional finite element methods (FEM) [13] fall short when applied to the brain's microenvironment. To model this subvolume alone with sufficient accuracy would require over 20 billion tetrahedra using a uniform FEM mesh. This volumetric meshing of a dense neuronal network with this resolution itself is hardly solvable, before even attempting any computations.

To address these limitations, we employ a matrix-free iterative boundary element fast multipole method (BEM-FMM) [14],[15],[16]. Its charge-based formulation [17],[18],[19] is readily applicable to computing induced electric charges on cell membranes and walls of blood vessels. These charges generate their own secondary electric field which alters the primary macroscopic field and changes the expected activating threshold of the neurons. Initial smaller-scale results are reported in [19],[20]. Still, they are not directly applicable to larger brain networks since the typical academic computer hardware limits the total number of degrees of freedom to ~ 0.1-0.2 billion. To mitigate this constraint, a nested iterative solution is developed in this study, which has the advantage of a faster convergence, albeit at the cost of longer execution time.

The primary aims of our study are twofold. First, we perform quasistatic (as governed by the Laplace equation) electromagnetic field computations in a highly complex medium (microscopic brain tissue) with Neumann (insulating) boundary conditions imposed on cell membranes and walls of the blood vessels. Second, biophysical analysis is carried out based on the fundamental cable equation [21],[22],[23], neuron morphologies precisely linked to the physical neurons, and known ion channel models for rodents [24],[6],[7],[8]. The brain sample under study [4],[5] is considered as it stands i.e., no cloning, elongation, or scaling neuronal processes and capillaries of any kind are used. The goal is to modify the activating function of the cable equation by the field perturbations found from the electromagnetic analysis and perform a detailed biophysical analysis similar to that of [6],[7],[8] to establish new neuronal activating thresholds.

2. Materials and Methods

2.1 MICrONS L2/L3 dataset of mouse visual cortex

The starting point is a semi-automated reconstruction of the L2/3 P36 male mouse primary visual cortex volume of approximately 250×140×90 μm (Fig. 1a) from electron microscopic images with a resolution of 3.6×3.6×40 nm (Fig. 1b). This reconstruction includes physical (not skeletonized) pyramidal and non-pyramidal neurons, astrocytes, microglia, oligodendrocytes and precursors, pericytes, vasculature, nuclei, mitochondria, and synapses [4],[5]. In total, 364 excitatory (Fig. 1f) and 32 inhibitory (Fig. 1g) neurons with cell bodies within the volume (Fig. 1c,e) were segmented, along with some microvasculature (Fig. 1d) [5]. For 301 neurons, the labeled neuronal centerlines (skeletons) in the common `swc` format were also made available [5]. This provides a unique opportunity to estimate the effect of the local field perturbations using biophysical analysis [25].

2.2 Data post-processing and computational testbed

Only the neurons themselves and the vasculature (with a few astrocytes) – the major perturbers of the impressed or primary electric field $\boldsymbol{E}_{\mathrm{e}}^{i}$ – were included into the present numerical analysis. Numerous neuroglia cells seen in Fig. 1b were not included in the analysis due to their small size, which made them impossible to model, even with advanced numerical simulation tools. The volume occupied by these microstructures (extracellular space) was considered approximately homogeneous. The volumetric fraction of the neuronal cells within the brain volume was estimated in Table S1 of Suppl. A as ~30±5% by computing the volume of each neuron and taking into account neuronal mesh intersections (below). This is less than the previously reported values on the order of ~70% [27],[28],[29] (Suppl. A) since all neurons with somas outside of this relatively small sample were omitted and their dendritic/axonal processes, which are still within the sample, were ignored.

Suppl. A describes the post-processing procedure for the original sample and its results. Based on this data, Table S1 of Suppl. A lists major topological and biophysical parameters of the created computational testbed, including estimated sample anisotropy. Both the facet size for membrane discretization (Fig. 2a) and the skeleton's spatial resolution (Fig. 2b,c) for the biophysical analysis were kept at approximately 100 nm to resolve large yet very localized variations of the impressed field due to multiple nearfield interactions of the neuronal processes as well as multiple intersections of neuronal arbors of different neurons (Section 2.3 below).

2.3 Mesh intersections and their resolution

The neuronal and vasculature surface meshes so constructed were found to heavily intersect with each other at multiple locations (cf. Fig. S2 of Suppl. B). These intersections reflect true synaptic interconnections between different neurons with a list of 1,960 synapses established in [26]. At the same time, some of the intersections are likely due to the imprecise segmentation and subsequent, not entirely identical, remeshing. Fig. 2d illustrates the most common intersections – interconnections – including the dendrite to dendrite and axon to dendrite intersections. Two different colors correspond to the two different neurons. Fig. 2e illustrates the less common intersections – dendrite to soma and axon to axon, respectively. Additionally, Suppl. B demonstrates an intersection map between neighboring excitatory neurons #238 and #290, respectively (Fig. S2). Fig. S2 also presents a mesh intersection roster of excitatory neuron #238 with all other neurons of the sample. It is observed that neuron #238 intersects with almost all neurons of the sample. Similar and even more dramatic results were observed for other larger neurons within the sample.

To resolve the mesh intersections numerically, we used the method illustrated in Fig. 2f,g. For two intersecting processes from Fig. 2f, all triangles belonging to either process and having at least one node within another process (mesh) have been removed. This operation does not exactly join the two meshes but leaves a gap in between as seen in Fig. 2g. When the gap size is small compared to the intersection domain itself, which is achieved by a fine mesh resolution, the gap has a minor influence on the results as demonstrated by our refined mesh computations (Suppl. B).

2.4 Computing extracellular electric field and extracellular potential

For the computation of the extracellular electric field, the approach developed in two relevant yet smaller-scale studies [19],[20] has been used. It assumes that the membrane is non-conducting (insulating) at the end of initial polarization [30],[31],[32]. The same condition applies to the walls of the blood capillaries. The condition of the insulating membrane makes it possible to fully decouple the extracellular solution in the form of a classic uniquely solved exterior problem with the simple Neumann (zero normal current density) boundary conditions at the outer surface of the membrane.

In response to an impressed or primary extracellular field $\boldsymbol{E}_{\mathrm{e}}^{i}$ with the (local) potential φ_{e}^{i}, induced surface charges will accumulate on the membrane surfaces. The secondary field of these charges, $\boldsymbol{E}_{\mathrm{e}}^{s}$, will alter the extracellular electric field. The total field in the brain will become $\boldsymbol{E}_{\mathrm{e}} = \boldsymbol{E}_{\mathrm{e}}^{i} + \boldsymbol{E}_{\mathrm{e}}^{s}$ and the total extracellular potential will become $\varphi_{\mathrm{e}} = \varphi_{\mathrm{e}}^{i} + \varphi_{\mathrm{e}}^{s}$. The goal of the electromagnetic part of the modeling pipeline is to find the secondary field and potential. We have applied a uniform electric field $\boldsymbol{E}_{\mathrm{e}}^{i}$ with the amplitude of 100 V/m for each independent field polarization (x, y, z).

This single-layer charge formulation allows for direct application of the charge-based boundary element fast multipole method (BEM-FMM) [17],[18],[19],[20]. The BEM-FMM is ideal for this type of problem since it does not require construction of an explicit system matrix and does not require a volumetric mesh for the complicated interior/exterior domains. For the present case, however, the BEM-FMM was only capable of computing the field of ~100 interacting neurons (with ca 0.15 billion facets) simultaneously. For larger samples, it required a prohibitively large RAM more than 1 TB and was experiencing slower convergence of the underlying GMRES algorithm [33].

Therefore, a nested iterative method has been developed and is illustrated in Fig. 3a. At initial step 1, each neuron is solved in isolation and is not affected by charges deposited on other neurons. The membrane charge deposition in response to the impressed field $\boldsymbol{E}_{\mathrm{e}}^{i}$ (or the self-interaction) is found via the standard iterative BEM-FMM solution for every neuron in homogeneous space. At step 2, the primary field $\boldsymbol{E}_{\mathrm{e}}^{i}$ is modified by the field of charges deposited on other neurons found in step 1. The membrane charge deposition for every neuron is recomputed with this modified primary field. The process repeats itself until a convergence criterion is met. The corresponding convergence curves (Fig. 3b,c) indicate a sub-percent error for the collinear electric field at the neuronal centerlines after 6 iterations. This method is potentially capable of modeling an unlimited number of cells, although CPU time now increases as $O(N^2)$ where N is the total number of cells. Electromagnetic computational results of this study required approximately 2 months of continuous CPU time when simultaneously utilizing 7 terminal servers and multiple nodes of a high-performance computing cluster.

2.5 Extracellular potential at centerlines/skeletons of neuronal processes

The activating function of the one-dimensional cable equation [21],[22],[23] needs extracellular potential or the collinear extracellular electric field at the centerlines of neuronal processes in the form of infinitesimally thin, transparent “wires”. For finite-thickness neuronal process, these values are extracellular fields averaged over the cross-section. In the extracellular domain (and only there), the field solution obtained previously is equivalent to the solution for the entirely non-conducting interior. Therefore, the averaged values are most accurately obtained when the field and the

potential are directly computed at the centerlines using the same extracellular solution which simultaneously holds for the entirely non-conducting interior [19],[20].

An appealing result of this solution is that both the transmembrane potential and the double layer density at the end of initial polarization are obtained automatically. Once the extracellular potential φ_{e} is known, we subtract its value from the constant resting potential value inside the cell and obtain the transmembrane potential φ_{m}. Its product with the electrical permittivity of the membrane is the density of the double layer of charges across the cell membrane.

2.6 Biophysical modeling

We implemented rodent neuron models developed in Refs. [24],[6],[7],[8] with 6 active channels for the soma, 8 active channels for the axons, 1 active channel for the basal dendrites, and 3 active channels for the apical dendrites initially developed and used by Aberra et al. [6]. The NEURON Software [25] with fine spatial and temporal resolutions has been employed to study neural activation in response to the extracellular potential/electric field computed previously at the centerlines of the neuronal processes. The neuron morphology for 267 available neuron models (including soma, axons, apical and basal dendrites) was loaded into NEURON by its Import3D tool. The implementation for the most important axonal channels was additionally verified against in-house MATLAB-based biophysical software. Every neuron was modeled independently, following the approach of Refs. [6],[7],[8]. Intercellular communications were not yet considered.

We used four stimulation pulse forms (Fig. S3 of Suppl. C): (i) a monophasic positive/negative rectangular pulse starting at $t = 0$ and with a duration of $0.1\ \mathrm{ms}$ and; (ii) an experimentally measured positive/negation biphasic TMS pulse with an overall duration of $0.3\ \mathrm{ms}$. The pulse amplitude gradually increased until the neuron activating criterion (the transmembrane voltage rises above zero anywhere in the arbor) was met. After that, the amplitude was decreased with a smaller step to pass the activating threshold in the opposite direction. This automated search procedure – the bisection method – requires approximately 15 steps and about 15-20 min per neuron on average. The overall simulation time for all neurons with x, y, and z polarizations, for all pulse forms, and for both primary and total extracellular fields/potentials did not exceed two CPU months. Other details of the biophysical modeling setup are described in Suppl. C.

The L2/L3 dataset does not provide information about axon myelination. However, the rodent axons are partially myelinated [6],[7],[8]. To account for this, we also modeled the case of artificial myelination. All axonal branches were assigned a myelin sheath with a thickness of 0.2 times the local radius. The nodes of Ranvier were placed at bifurcations, terminations, and along the segmental length, 20 µm apart from each other.

3. Results

3.1 Self-convergence of nested iterative BEM-FMM numerical solution

Fig. 3b,c shows solution convergence results (y-polarization of the primary field) for both the induced surface charge density (Fig. 3b) and the collinear electric field projected onto the centerlines of the neuronal processes (Fig. 3c). For every neuron labeled versus its height and every blood vessel appended at the end of the list, Fig. 3b gives a relative 2-norm error for the induced surface charge density between two subsequent iterations as well as the average relative error for all compartments. Fig. 3c provides similar results for the collinear electric field at the neuronal centerlines. One observes that 6 iterations are sufficient to obtain a sub-percent relative field error. An additional test of solution accuracy has been performed by comparison with the direct numerical solution for 22 neurons treated as a single network. The relative average field solution error versus the direct solution for the single network after six iterations was also below 5%.

3.2 Computed membrane charge deposition and induced surface charge density

Fig. 4 illustrates the induced surface charge density distribution for neuron #321 and its 200 nearest neighbors in the sagittal (left or a,c,e) and coronal (right or b,d,f) planes, respectively. The uniform primary field of 100 V/m is in the dorsal-ventral direction. Fig. 4a,b) is the case when only one neuron #321 is present (the self-interaction). Fig. 4c,d) is the induced surface charge density when all neurons and microcapillaries are present, which was obtained after 6 iterations. Fig. 4 e,f) depicts the induced surface charge density for neuron #321 and its 200 nearest neighbors in two principal planes. One observes that the charge deposition increases and becomes more nonuniform for the tightly spaced cells due to near-field interactions.

3.3 Computed collinear electric field at centerlines of neuronal processes for biophysical modeling

Fig. 5 illustrates the resulting effect of membrane charge deposition on the collinear electric field projected onto the centerlines of neuronal processes for the same neuron #321. The sagittal plane view is shown corresponding to Fig. 4a,c,e. Fig. 5a) is the electric field projection in homogeneous space, when the neuronal membrane is not present per se and the same unform impressed electric field of 100 V/m is applied along the y axis (from dorsal to ventral). Fig. 5b) is the electric field projection when all neuron membranes are present, and the primary field is distorted by the field of the induced charges. One observes that perturbations of the collinear field are quite significant. Moreover, they are constructively or “in phase” accumulated in space so that a positive perturbation is added to the originally positive field projection and vice versa. This observation is explained in the Discussion section; it will have a major influence on the obtained results.

3.4 Solving cable equation. Reduction of neuronal activating thresholds

Fig. 6b) illustrates the activating threshold reduction factors. We choose the first 90 neurons with the longest non-cut axonal arbors in excess of 0.5 mm (Suppl. A). The neurons have been renumerated versus the axonal arbor length in descending order. The results are given for three polarizations of the primary electric field: medial-lateral (red), dorsal-ventral (green), and anterior-posterior (blue) and for the $0.1\ \mathrm{ms}$ rectangular negative stimulating pulse. The reduction factor is defined as the ratio of the activating threshold of a physical neuron within the brain (with the total field $\boldsymbol{E}_{\mathrm{e}}$ and the total potential φ_{e}) to the activating threshold of the neuron skeleton in the homogeneous space (subject to the field $\boldsymbol{E}_{\mathrm{e}}^{i}$ and the potential φ_{e}^{i}). Fig. 6c gives the absolute activating thresholds for the corresponding 90 neuron skeletons in homogeneous space. Fig. 6d gives the absolute activating thresholds for 90 physical neurons within the sample. The units in Fig. 6c,d are in terms of the field strength of 100 V/m; one unit corresponds to 100 V/m. Figs. S4-S7 of Suppl. C give the same data for the remaining pulse forms and for myelinated axons (Fig. S7). The last figure was again computed for the rectangular negative $0.1\ \mathrm{ms}$ long pulse. Average threshold reduction factors for all pulse forms/polarizations of $\boldsymbol{E}_{\mathrm{e}}^{i}$ are given in Table 1 (non-bold entries).

In Fig. 6 and Figs. S4-S7 of Suppl. C, one observes substantially different threshold reduction factors for three different polarizations (directions) of the primary field. This fact is further explained by the moderate anisotropy of the brain sample. We can characterize the anisotropy as an equivalent straight fiber density distribution of the sample (Suppl. A). Fig. 6a schematically illustrates the equivalent straight fiber density distribution of the brain sample under study.

3.5 Results for threshold reduction factors for different polarizations of primary field

Table 2 summarizes normalized standard deviation of the average neuronal activating thresholds for three different polarizations of the primary electric field. The first 90 neurons with the longest axonal arbor have been processed. One observes that the normalized standard deviation between average thresholds for different directions of the applied primary field is generally smaller for the brain sample as compared to individual neuron skeletons in homogeneous space; the cell membrane interactions tend to make brain stimulation more “equal” in all directions.

3.6 Strength-duration results

Fig. 7a illustrates a very weak dependency of the threshold reduction factor on the duration of the applied stimulation pulse. A case in point is neuron #348 within the brain when the negative rectangular pulse is applied. At the same time, the absolute values of the activating threshold indeed follow the classic strength duration dependency [34] with a high degree of accuracy (cf. inset in Fig. 7a, note that a log-log scale has been used).

3.7 Dynamics of threshold reduction factor

Fig. 7b,c,d illustrates the threshold reduction factor dynamics as a function of the number of neighboring cells included in the computations. For each of three representative neuron cells (#238, 321, 348, all having different lengths of axonal arbor), we start adding its nearest neighbors (0, 5, 10 neighbors, etc.) from the entire brain sample and then repeat both electromagnetic and biophysical computations to find new activating thresholds. The x-axis is the corresponding relative volumetric fraction of neuronal mass computed using known volumes of each cell. The first point of every curve is the threshold reduction factor without neighbors, which is due to self-interaction of the neuron itself; the last point is the result for complete brain sample.

3.8 Extrapolation of threshold reduction factor to more realistic neuronal density

The volumetric fraction of the neuronal cells within the volume was estimated in Table S1 (Suppl. A) as ~30%. This is less than the known value of ~60-70% [27],[28],[29] in rats and mice since all neurons with somas outside the brain sample were omitted and their dendritic/axonal processes, which are still within the sample, were ignored. The threshold reduction factor curves in Fig. 7b,c,d could in principle be extrapolated (as shown by dashed lines in Fig. 7b,c,d) to estimate the threshold reduction factor for the likely more realistic volumetric neuronal fill factor of 70% (shown by a red vertical line in Fig. 7b,c,d). Average extrapolated threshold reduction factors for all pulse forms and all polarizations of $\boldsymbol{E}_{\mathrm{e}}^{i}$ are also collected in Table 1 (bold font). These data were obtained by averaging extrapolated results for 5 neurons (#238, 261, 321, 333, and 348) with different lengths of axonal arbor and applying the corresponding slopes to all previously obtained average threshold reduction factors from Table 1 (non-bold entries).

4. Discussion

4.1 Threshold reduction mechanism explained with the help of a simple example-constructive accumulation of field perturbations when projected onto centerlines

Fig. 8 shows total electric field (electric current for the conductivity of 1 S/m) computed around cross-sections of a) one, b) two closely-spaced, and c) two more closely-spaced straight insulating cylinders. The impressed field $\boldsymbol{E}_{\mathrm{e}}^{i}$ has the value of 100 V/m or 100% and is directed from left to right along the x direction. In a), the maximum field of 200 V/m or 200% (a twofold field increase) appears exactly at the boundary; in b), the field between the two cylinders approaches 300 V/m. Different contour levels indicate field percentage changes (in V/m if the impressed field is 100 V/m). The paths of neuronal processes affected by these local field perturbations are shown by white arrows.

In Fig. 8, field perturbations are only significant at small distances on the order of the cross-sectional size of a cylinder (another axon or capillary). These local field perturbations are generally dipolar in nature. Local field increases are interchanged with the local decreases and vice versa, isotropically in space. It may therefore appear at first sight that the microscopic field perturbations of neighboring neurons or cells effectively cancel out, with no net effect on the activating thresholds.

We hypothesize, however, that the local field perturbations become nearly monopolar for axons whose centerline paths are directed approximately parallel or antiparallel to the projection of the impressed electric field. These “easily excitable” axons are likely most important and influential to the overall solution. For instance, the positive projected field of axonal path 1 in Fig. 8a further increases when passing any nearby perturbating processes. Similarly, the negative projected field of axonal path 2 in Fig. 8a further decreases when passing any nearby perturbating processes. In both cases, the electric field *increases* in magnitude as the axon passes the perturber. This is indeed not true for axons 3 and 4 in Fig. 8a. However, these axons are likely not excited in any way since their projected fields approach zero. Similar observations are held for axons in Fig. 8b,c.

Fig. 5b obtained for the actual neuron within the brain clearly demonstrates the same effect: field perturbations are constructively accumulated in space when projected onto the centerlines of neuronal processes so that a positive perturbation is added to the originally positive field projection (red and yellow) and a negative perturbation is added to the negative projection (blue and cyan).

To demonstrate the value of this effect, we consider in Fig. 8d a simple classic activating *E*-field profile along axonal path s [21],[22],[23]. A nearby electrode (cathode) generates the extracellular potential $\varphi_e^i(s) = \varphi_0/\sqrt{1+(s/s_0)^2}$, $\varphi_0 < 0$ which can be obtained by integrating the electric field along the path. A similar profile could occur for a bent axon in a unform electric field (cf. a loop marked by a white arrow in Fig. 5b). Due to the nearby cells, this field will be distorted as shown in Fig. 8e. After integrating the total collinear electric field, a lower depolarization potential is obtained than that for the primary extracellular field as shown in Fig. 8f (black vs. red). This results in easier activation and a potentially lower activating threshold. Similar reasoning holds for neuronal bifurcations and terminations. The corresponding experimental proof for a straight axon between two macroscopic cylinders can be found in [35].

4.2 Different threshold reduction factors are due to brain sample anisotropy

Fig. 6, Figs. S4-S7 of Suppl. C, and Table 1 predict different activating threshold reduction factors for different directions of the impressed electric field in the mouse visual cortex. The average reduction factor is: strongest (0.55) in the dorsal-ventral direction with the sparsest equivalent straight fiber density of $0.9e5\ \mathrm{mm}^{-2}$; medium (0.76) in the anterior-posterior directions with the

medium equivalent straight fiber density of $1.0e5\ \mathrm{mm}^{-2}$; and lowest (0.85) in the medial-lateral direction with the densest equivalent straight fiber density of $1.3e5\ \mathrm{mm}^{-2}$. According to the previous section, the threshold reduction factor is mainly due to near-field interactions or "intersections" with the perpendicular fibers – cf. Fig. 6a. For fibers in the dorsal-ventral direction, the number of such intersections per unit length in Fig. 6a is the highest and is proportional to the fiber density in the two other directions, i.e. to $1.0e5 \times 1.3e5$. For fibers in the anterior-posterior direction, the number of such intersections per unit length in Fig. 6a is medium; it is again proportional to the fiber density in two remaining directions, i.e. to $0.9e5 \times 1.3e5$. Finally, for fibers in the medial-lateral direction, the number of such intersections per unit length in Fig. 6a is the lowest and is proportional to the fiber density in two other directions, i.e. to $0.9e5 \times 1.0e5$. These three numbers of intersections per unit length relate as 1.0, 0.90, and 0.70 when normalized to their largest value. On the other hand, the inverse normalized threshold reduction factors for the three polarizations cited above relate as 1.0, 0.72, and 0.65 when normalized to the largest value. Qualitive agreement between the two sets of numbers becomes obvious.

4.3 Microscopic field interactions tend to undo the effect of brain sample anisotropy

A further observation as best seen in Fig. 6d and Fig. S7d of Suppl. C is that the microscopic field interactions tend to equate neuron activating thresholds for different directions of the applied stimulation field (cf. also Table 2). The reasoning of the previous section could again be used to explain this effect.

4.4 Effect of blood vessels

Separate electromagnetic and biophysical computations with and without blood vessels have been performed for the y-polarization of the primary impressed field and for the rectangular negative stimulation pulse with the duration of $0.1\ \mathrm{ms}$. It was found that the microcapillaries are responsible for changing the average activating threshold reduction factor from 0.79 (no blood network) to 0.76 (Table 1) when blood vessels are present. Note that segmenting the brain blood supply network was not the major priority of the L2/L3 MICrONS project [4],[5]. As such, we may expect a higher influence when all microcapillaries and astrocytes are carefully included within the much larger $1\mathrm{mm}^3$ MICrONS mouse brain sample [36],[37].

4.5 Size of brain sample is too small to predict absolute activating threshold values

The small size of the L2/L3 brain sample leads to cutting out a large portion of the neuronal processes, most notably axon collaterals. Our computations show that the absolute activating threshold values are severely affected by this operation. Additionally, the arguably most sensitive excitatory neurons of L5 [7] are not included into the sample. This is perhaps why the absolute

threshold values in Fig. 6 and Figs. S4-S7 (Suppl. C) overestimate the experimentally measured value of 90 V/m in mouse primary motor cortex (Suppl. D) very significantly. Even in the most favorable case of myelinated axons, there are only nine neurons with the activating threshold below 200 V/m (Fig. S7d, Suppl. C) and none of them has the activating threshold below 100 V/m.

4.6 Size of brain sample may be sufficient to correctly predict relative threshold reduction factors

A simple numerical experiment with 20 neurons having the longest axonal arbors and the average arbor length of 2.5 mm versus 90 neurons having the longest axonal arbors and the average arbor length of 1.4 mm shows that the *relative* threshold reduction factors remain nearly the same in both cases, to within 3%. This is valid for all polarizations and all pulse forms. While the average axonal length reduces by 44% in this example, the threshold reduction factors change by less than 3%. Thus, the relative threshold reduction factors weakly depend on the retained arbor length.

4.7 Other limitations of this study

Our biophysical modeling treats all neuronal cells independently, following previous work [6],[7],[8] to demonstrate the impact of realistic microscopic structures on direct neuron activation threshold. On the other hand, the L2/L3 brain sample is already supplied with a list of 1,960 synapses between 334 excitatory pyramidal cells [5] obtained in [26] allowing future extension of our approach simulating network/synaptic modulation. Though used ubiquitously, there are inherent limitations of the one-dimensional cable equation, especially close to the large soma. Modern bidomain models [39],[40] could possibly resolve this issue. The next logical yet extremely challenging step is to analyze the much larger 1mm^3 MICrONS mouse brain sample [36], which includes a considerably better-developed axonal arbor and ~75,000 neurite cells. This would require further improvement of the computational method.

Our results should be extrapolated with caution to humans. It is reasonable to expect that the same trends would be observed if performing analogous computational analysis for a human tissue sample, however given different sizes and packing densities of cells (as well as the size of the tissue block itself), the exact numerical factors might differ. Notwithstanding these limitations, the present study provides the methodology for addressing all these issues.

5. Conclusions

A method is proposed to model perturbations of an impressed electric field within a microscopically realistic brain, with many tightly spaced neuronal cells and blood microcapillaries. This impressed field is due either to brain stimulation or to a firing cluster of neurons themselves. For the first time,

we have been able to model the relatively sizable fully anatomical mouse brain sample containing ~400 detailed neurite cells and blood microcapillaries in detail.

Electromagnetic modeling was coupled with biophysical modeling that is based on neuron morphologies precisely linked to the physical neurons and known ion channel models for rodents. No cloning, elongation, or scaling neuronal processes and capillaries of any kind were used.

The method is applied to predict changes in neuron activating thresholds caused by microenvironment. We observed and justified activating threshold reduction factors of 0.85–0.55 on average for different directions of the impressed field and different representative stimulation pulse forms. The obtained results are clearly explainable and are consistent across the wide range of brain stimulation conditions. The application of the presented multi-scale modeling framework spans all forms of electromagnetic brain stimulation.

Acknowledgements

Authors express their gratitude to Dr. Bethanny Danskin and the Virtual Observatory of the Cortex (VORTEX) program of the Allen Institute for Brain Science for their assistance in processing the L2/L3 brain sample, to Dr. Ted Carnevale of Yale School of Medicine for his guidance in utilizing NEURON software with superior spatial resolution, and to Dr. Padma Sundaram of Massachusetts General Hospital for useful discussions. Special thanks are extended to Dr. Ermal Toto and Dr. James Kingsley of Academic and Research Computing at Worcester Polytechnic Institute for their support in assembling and executing highly demanding parallel computational tasks. This study has received support from the NIMH grant R01MH130490 and NIBIB grant R01EB035484 (SNM), NIDCD grant R01DC020891 (ARN), NINDS grant U24NS120053 (BD) as well as the Intramural Research Program of NIH, NIMH ZIAMH002955 (Z-DD), and Intramural Research Program of NIH, NIDA ZIADA000638 (HL). The content is solely the responsibility of the authors and does not necessarily represent the official views of the National Institutes of Health.

Tables and Figures

Table 1. Averaged relative reduction factor of the neuronal activating thresholds for different polarizations of the impressed (primary) electric field and different pulse forms (Suppl. C) between a neuronal skeleton in a homogeneous medium and the microscopically realistic brain, respectively. The first 90 neurons with the longest axonal arbors have been processed.

Modeling setup	Medial-lateral polarization of $\boldsymbol{E}_{\mathrm{e}}^{i}$	Dorsal-ventral polarization of $\boldsymbol{E}_{\mathrm{e}}^{i}$	Anterior-posterior polarization of $\boldsymbol{E}_{\mathrm{e}}^{i}$
A Monophasic rect. pulse, 100 µs, negative	0.92	0.81	0.67
B Monophasic rect. pulse, 100 µs, positive	0.90	0.85	0.68
C Biphasic pulse (TMS), 300 µs, negative	0.90	0.84	0.68
D Biphasic pulse (TMS), 300 µs, positive	0.89	0.85	0.68
E Same as A but with all axons myelinated	0.91	0.81	0.65
A Extrapolated to realistic neuronal density	**0.86**	**0.76**	**0.54**
B Extrapolated to realistic neuronal density	**0.85**	**0.72**	**0.55**
C Extrapolated to realistic neuronal density	**0.82**	**0.78**	**0.57**
D Extrapolated to realistic neuronal density	**0.81**	**0.78**	**0.54**
E Extrapolated to realistic neuronal density	**0.85**	**0.76**	**0.52**
Average	**0.85**	**0.76**	**0.55**

Table 2. Normalized standard deviation of the neuronal activating thresholds for three different polarizations of the primary electric field (Suppl. C). The first 90 neurons with the longest axonal arbors have been processed.

Modeling setup	Normalized STD, Homogeneous medium	Normalized STD, Microscopically realistic brain
A Monophasic rect. pulse, 100 µs, negative	0.18	0.04
B Monophasic rect. pulse, 100 µs, positive	0.35	0.23
C Biphasic pulse (TMS), 300 µs, negative	0.19	0.15
D Biphasic pulse (TMS), 300 µs, positive	0.15	0.14
E Same as A but with all axons myelinated	0.25	0.07

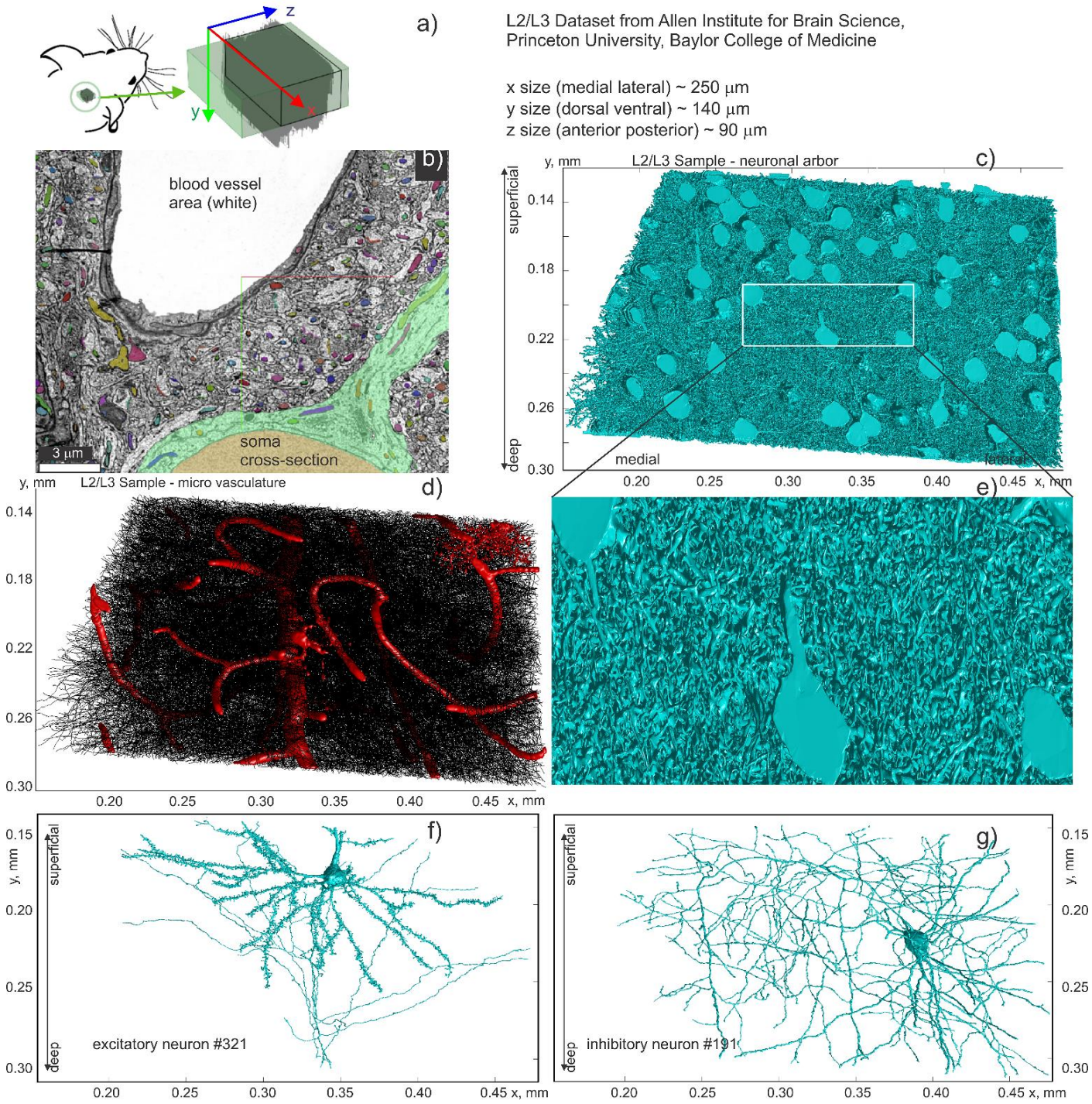

Fig. 1. a) L2/L3 Sample. b) Snapshot of a relative position of a mouse brain neuron (soma) vs. a nearby blood capillary (white area) within the sample [5], [4]. c) Segmented neuronal arbor of the entire sample. d) Centerlines/skeletons of individual neurons and segmented blood vessels in red (with an astrocyte at top right). e) Zoomed in arbor area from c). f,g) Excitatory and inhibitory neurons within the sample volume to scale. The axes differ from the mouse-centric coordinate system [4].

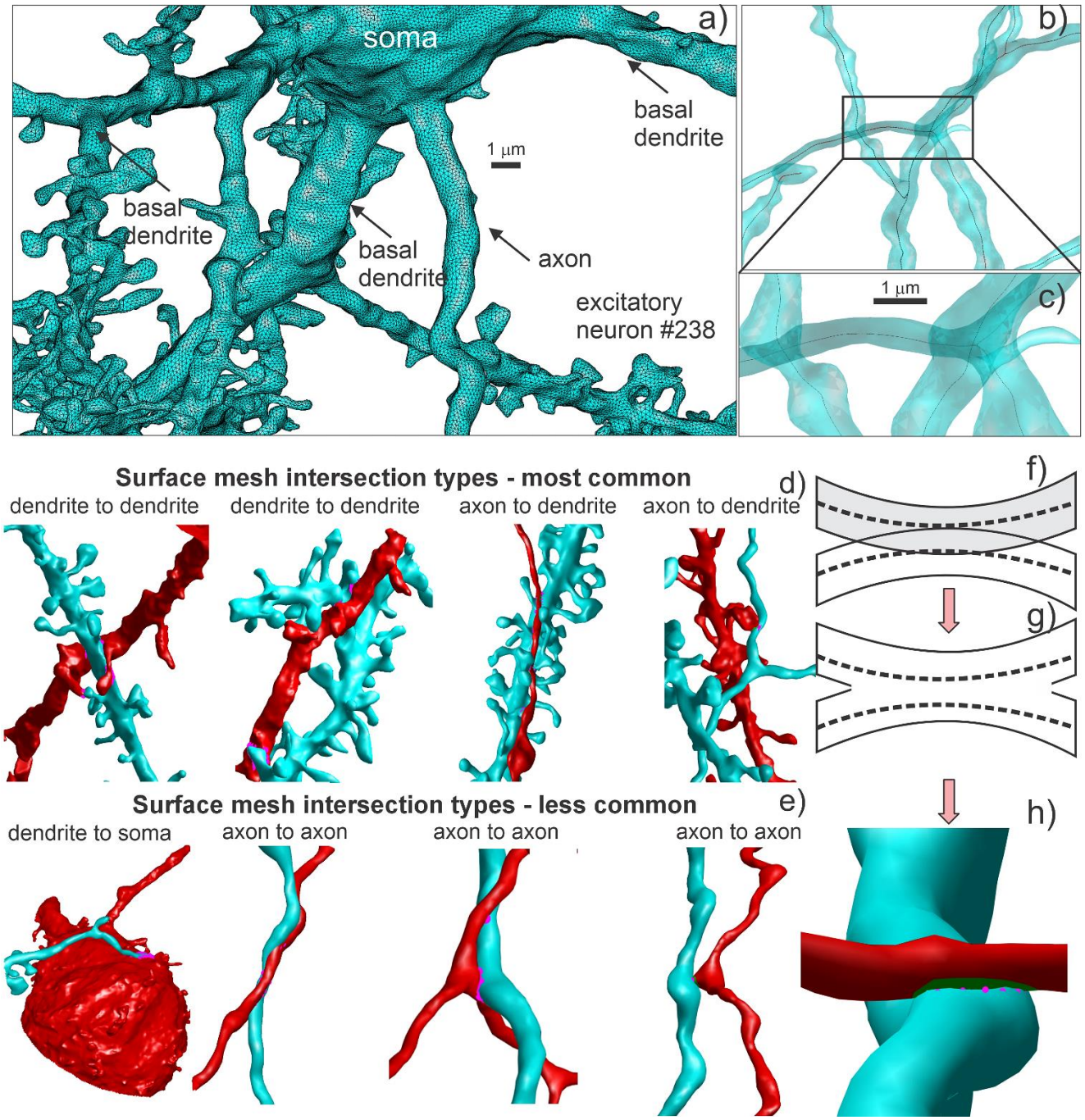

Fig. 2. a) Final high-quality membrane surface triangular mesh for neuron #238 which is located approximately in the middle of the sample. The membrane mesh has 2 million facets in total and a 100 nm resolution. b,c) Healed centerlines of a neuron. d) Most common intersections observed – dendrite to dendrite and axon to dendrite intersections. Two different colors correspond to the two different neurons. e) Less common intersections – dendrite to soma and axon to axon, respectively. f,g) Mesh intersection resolution via removal of inner triangles. h) Result of this operation for an axon-to-dendrite intersection. Removed triangular facets are marked dark green.

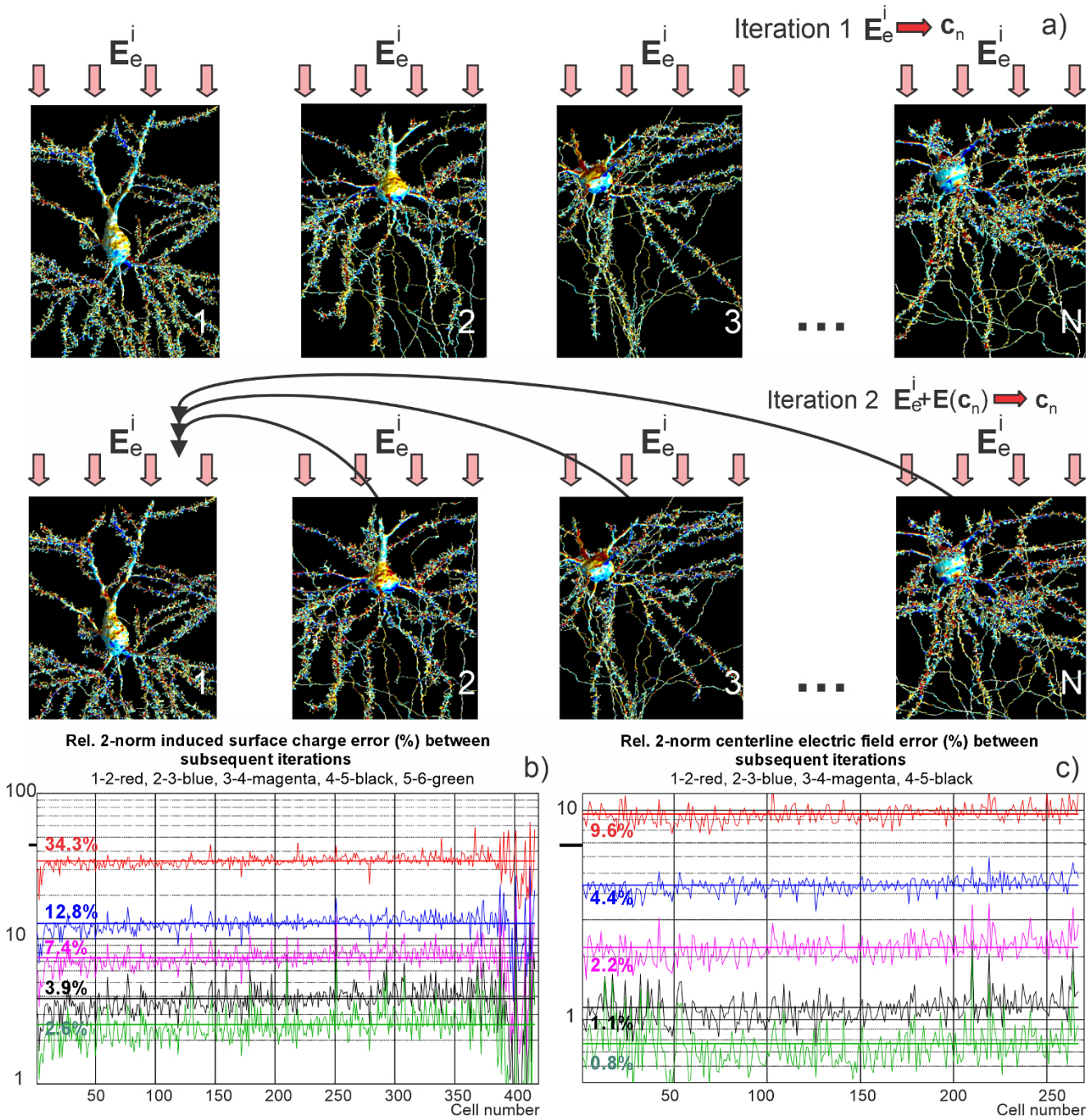

Fig. 3. a) Nested iterative solution method. At step 1, every neuron is considered independent. Membrane charge deposition in response to impressed or primary field $\boldsymbol{E}_{\mathrm{e}}^{i}$ is found via an iterative BEM-FMM solution. At step 2, the primary field $\boldsymbol{E}_{\mathrm{e}}^{i}$ is modified by the field of charges deposited on all other neurons. Membrane charge deposition for every neuron in response to this modified field is found next. The process further repeats itself until a convergence criterion is met. b) Convergence curves for the relative 2-norm surface charge density error. c) Convergence curves for the relative 2-norm error for the collinear electric field projected onto centerlines of neuronal processes.

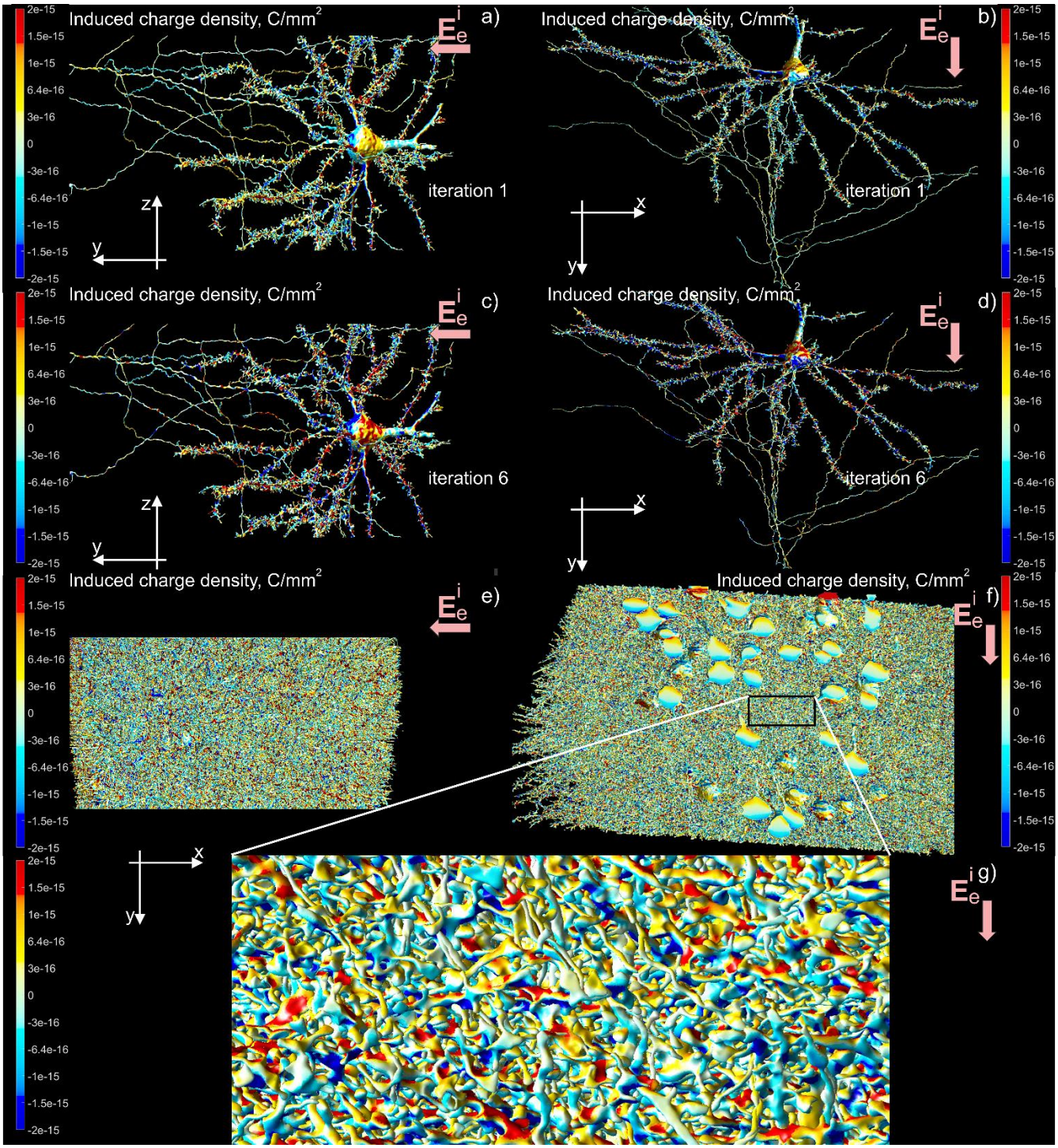

Fig. 4. Induced surface charge density for neuron #321 and its 200 nearest neighbors in sagittal (left or a,c,e) and coronal (right or b,d,f) planes. a,b) Induced charge density when only neuron #321 present (iteration 1 or self-interaction). c,d) Induced charge density when all neurons and microcapillaries are present (iteration 6). e,f) Induced surface charge density for 200 nearest neighbors. g) Zoomed in area of the brain sample.

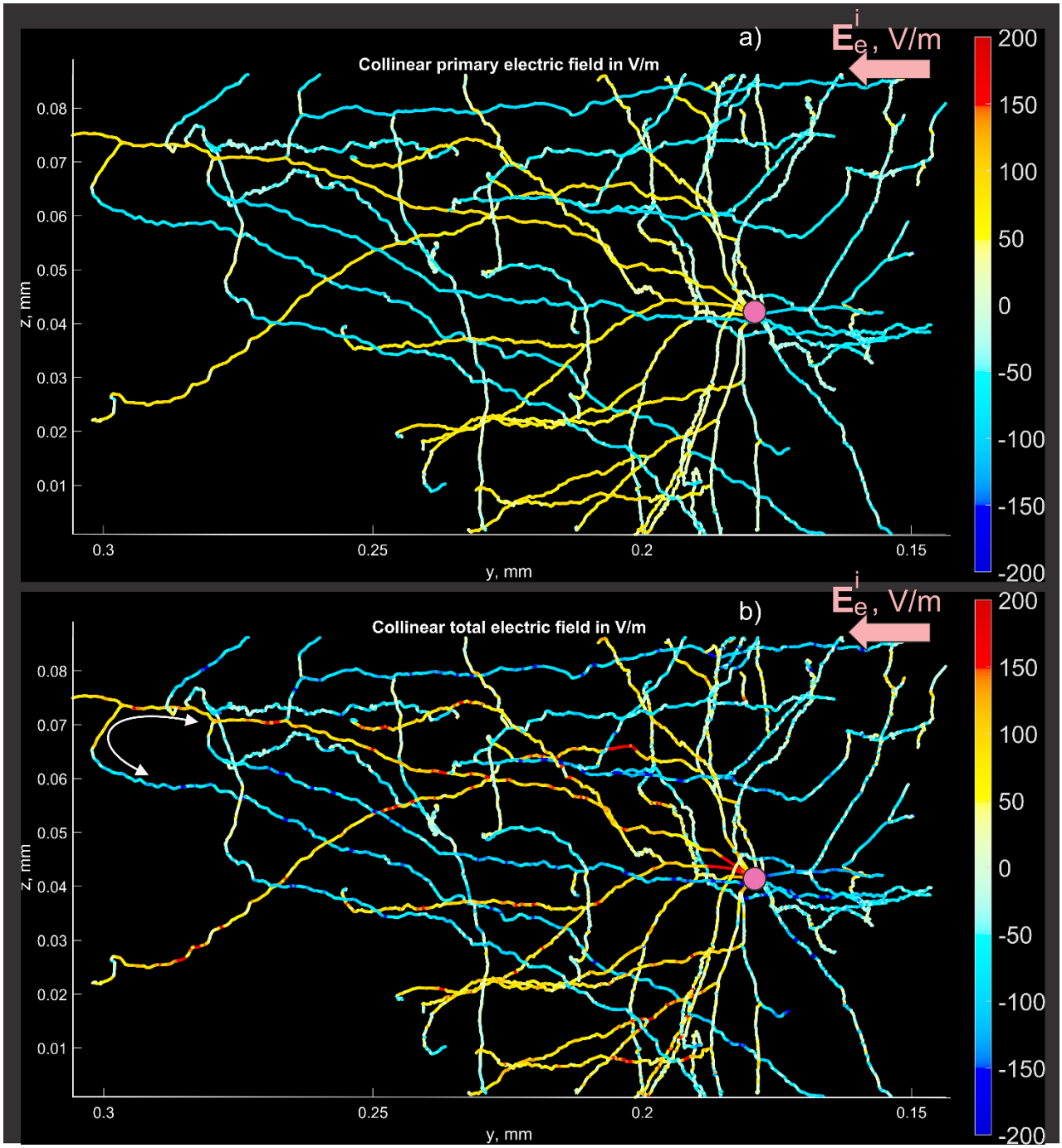

Fig. 5. Effect of membrane charge deposition on the collinear electric field projected onto the centerlines of neuronal processes for neuron #321. The sagittal plane view is shown corresponding to Fig. 4a,c,e. a) Electric field projection in homogeneous space, when the neuronal arbor is not present and a unform impressed electric field of 100 V/m is applied along the y axis (from dorsal to ventral). b) Electric field projection when all neurons are present, and the primary field is distorted by the field of the induced charges.

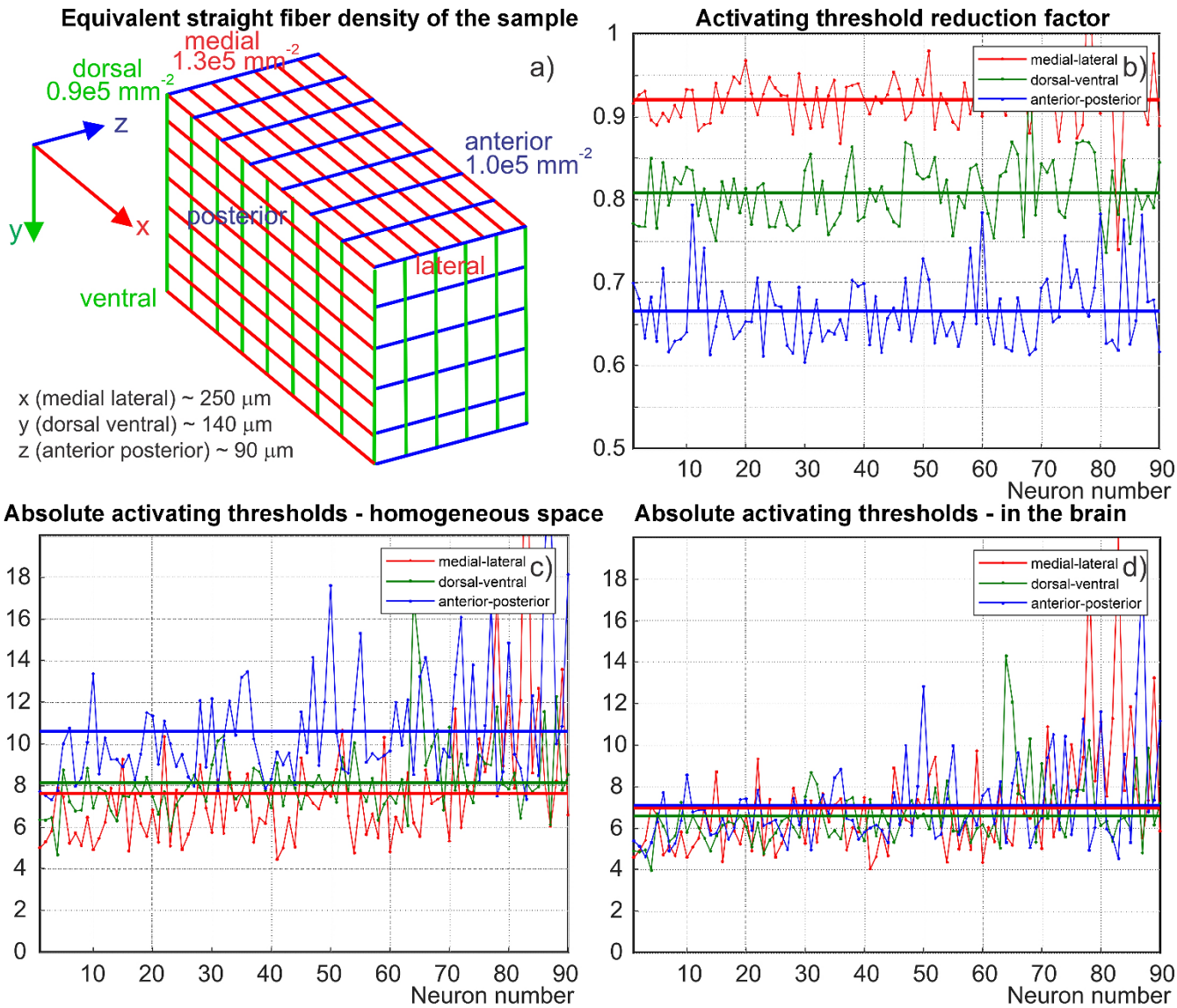

Fig. 6. a) Equivalent straight fiber density distribution of the sample characterizing its anisotropy. b) Activating threshold reduction factor for the first 90 neurons with the longest axonal arbors (sorted) for three polarizations of the primary electric field: medial-lateral (red), dorsal-ventral (green), and anterior-posterior (blue). c) Absolute activating thresholds for the same 90 neurons in homogeneous space. d) Absolute activating thresholds for the same 90 neurons within the sample. The units in c,d) are given in terms of the base field strength of 100 V/m; one unit corresponds to 100 V/m. These results are given for the case of the unmyelinated axonal arbor and a negative rectangular activation monophasic pulse with the duration of 0.1 ms. Results for all other cases are given in Suppl. C.

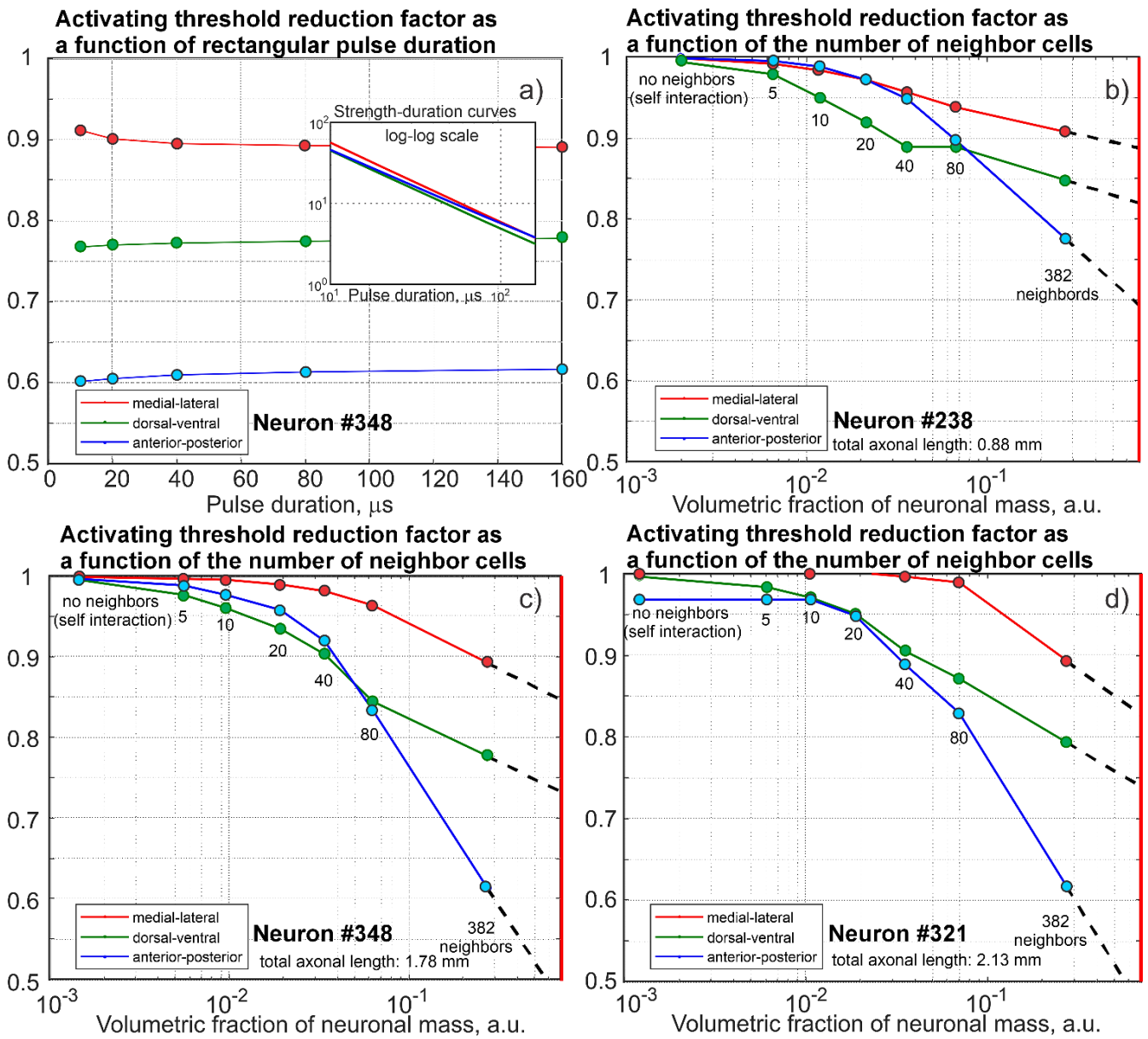

Fig. 7. a) Activating threshold reduction factor as function of rectangular negative pulse duration. The inset shows the corresponding strength-duration curves for neuron #348 within the brain sample. Inset units in are in terms of the initial field strength of 100 V/m; one unit corresponds to 100 V/m. b,c,d) Activating threshold reduction factors as function of the number of neighboring cells for three representative excitatory neurons with different lengths of the axonal arbor. All three neurons belong to the set of 90 neurons with the longest axonal arbor. The x-axis is the corresponding volumetric fraction of neuronal mass computed separately for each neuron when sequentially adding its neighboring cells. Red lines show the expected fraction of 70% [29]; dashed lines show expected linear extrapolation results.

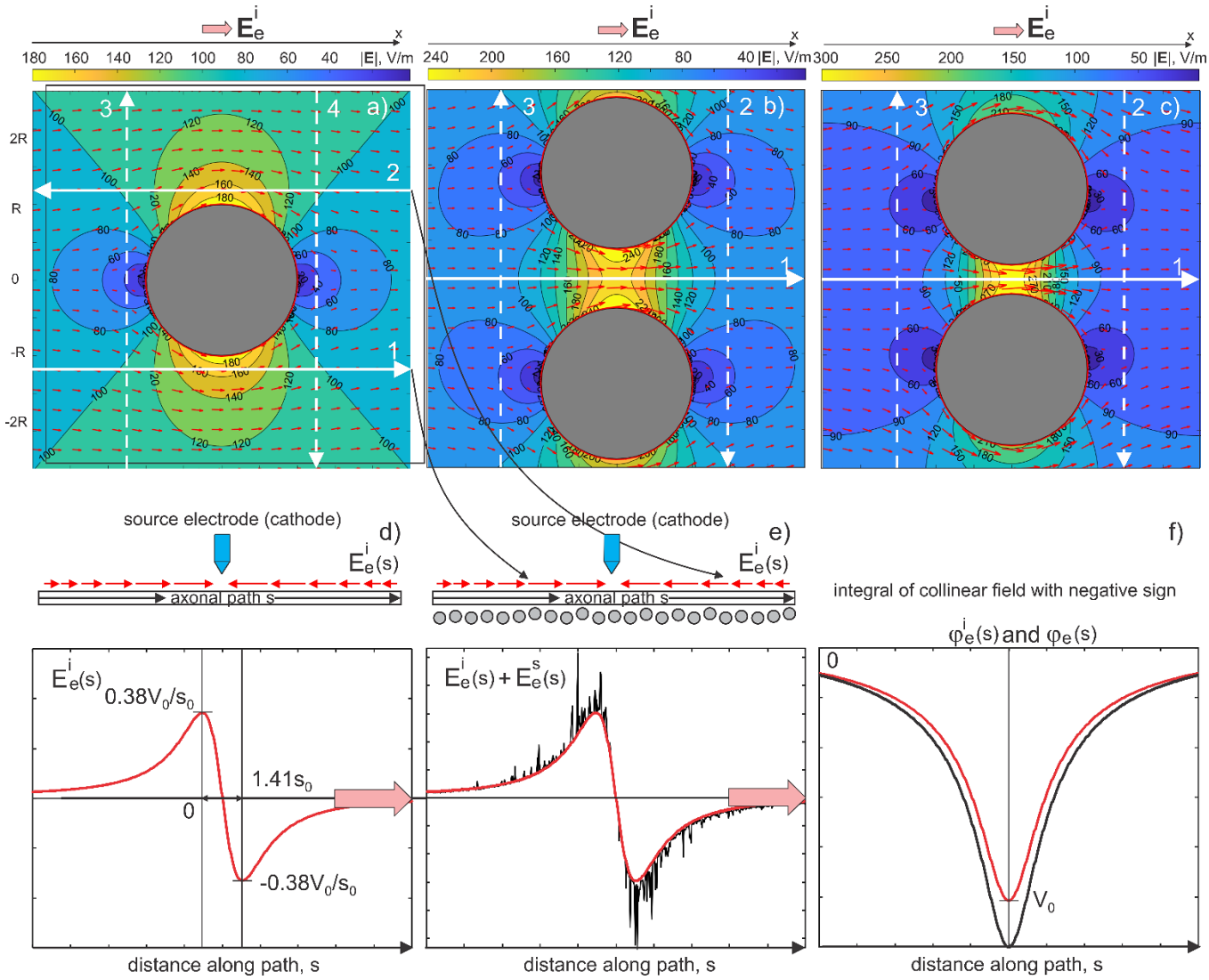

Fig. 8. Total electric field (electric current for the conductivity of 1 S/m) around cross-sections of a) one, b) two closely-spaced, and c) two more closely-spaced cylinders. The impressed field $\boldsymbol{E}_{\mathrm{e}}^{i}$ has the value of 100 V/m or 100% and is directed from left to right along the x direction. In a), the maximum of 200 V/m (a twofold field increase) appears exactly at the boundary; in b) the field between the two cylinders approaches 300 V/m. Different contour levels simultaneously indicate field percentage changes. d) Impressed collinear field $E_{\mathrm{e}}^{i}(s)$ along a straight axonal path s generated by an electrode. e) Constructive or "in phase" addition of secondary collinear field (black) to the primary collinear field (red). f) Further decrease of the extracellular depolarization potential $\varphi_e(s)$ (black) obtained after integrating collinear field along the path and enabling easier activation (or a lower activating threshold) as compared to the homogeneous case (red).

References

[1]. Siebner HR, Funke K, Aberra AS, Antal A, Bestmann S, Chen R, Classen J, Davare M, Di Lazzaro V, Fox PT, Hallett M, Karabanov AN, Kesselheim J, Beck MM, Koch G, Liebetanz D, Meunier S, Miniussi C, Paulus W, Peterchev AV, Popa T, Ridding MC, Thielscher A, Ziemann U, Rothwell JC, Ugawa Y. Transcranial magnetic stimulation of the brain: What is stimulated? - A consensus and critical position paper. Clin Neurophysiol. 2022 Aug;140:59-97. doi: 10.1016/j.clinph.2022.04.022.

[2]. Liu A, Vöröslakos M, Kronberg G, Henin S, Krause MR, Huang Y, Opitz A, Mehta A, Pack CC, Krekelberg B, Berényi A, Parra LC, Melloni L, Devinsky O, Buzsáki G. Immediate neurophysiological effects of transcranial electrical stimulation. Nat Commun. 2018 Nov 30;9(1):5092. doi: 10.1038/s41467-018-07233-7.

[3]. Deng ZD, Argyelan M, Miller J, Quinn DK, Lloyd M, Jones TR, Upston J, Erhardt E, McClintock SM, Abbott CC. Electroconvulsive therapy, electric field, neuroplasticity, and clinical outcomes. Mol Psychiatry. 2022 Mar;27(3):1676-1682. doi: 10.1038/s41380-021-01380-y.

[4]. Turner NL, Macrina T, Bae JA, Yang R, Wilson AM, Schneider-Mizell C, Lee K, Lu R, Wu J, Bodor AL, Bleckert AA, Brittain D, Froudarakis E, Dorkenwald S, Collman F, Kemnitz N, Ih D, Silversmith WM, Zung J, Zlateski A, Tartavull I, Yu SC, Popovych S, Mu S, Wong W, Jordan CS, Castro M, Buchanan J, Bumbarger DJ, Takeno M, Torres R, Mahalingam G, Elabbady L, Li Y, Cobos E, Zhou P, Suckow S, Becker L, Paninski L, Polleux F, Reimer J, Tolias AS, Reid RC, da Costa NM, Seung HS. Reconstruction of neocortex: Organelles, compartments, cells, circuits, and activity. *Cell.* 2022 Mar 17;185(6):1082-1100.e24. doi: 10.1016/j.cell.2022.01.023.

[5]. MICrONs Consortium et al. Functional connectomics spanning multiple areas of mouse visual cortex. *bioRxiv* originally published 2021.07.28.454025/updated 2023.04.19; doi: https://www.biorxiv.org/content/10.1101/2021.07.28.454025v3.

[6]. Aberra AS, Peterchev AV, Grill WM. Biophysically realistic neuron models for simulation of cortical stimulation. J Neural Eng. 2018 Dec;15(6):066023. doi: 10.1088/1741-2552/aadbb1.

[7]. Aberra AS, Wang B, Grill WM, Peterchev AV. Simulation of transcranial magnetic stimulation in head model with morphologically-realistic cortical neurons. Brain Stimul. 2020 Jan-Feb;13(1):175-189. doi: 10.1016/j.brs.2019.10.002.

[8]. Weise K, Worbs T, Kalloch B, Souza VH, Jaquier AT, Van Geit W, Thielscher A, Knösche TR. Directional Sensitivity of Cortical Neurons Towards TMS Induced Electric Fields bioRxiv 2023.07.06.547913; doi: https://doi.org/10.1101/2023.07.06.547913.

[9]. Bingham CS, McIntyre CC. Subthalamic deep brain stimulation of an anatomically detailed model of the human hyperdirect pathway. J Neurophysiol. 2022 May 1;127(5):1209-1220. doi: 10.1152/jn.00004.2022.

[10]. Noor MS, McIntyre CC. Biophysical characterization of local field potential recordings from directional deep brain stimulation electrodes. Clin Neurophysiol. 2021 Jun;132(6):1321-1329. doi: 10.1016/j.clinph.2021.01.027.

[11]. Bower KL, McIntyre CC. Deep brain stimulation of terminating axons. Brain Stimul. 2020 Nov Dec;1 3(6):1863-1870. doi: 10.1016/j.brs.2020.09.001.

[12]. Ye H, Steiger A. Neuron matters: electric activation of neuronal tissue is dependent on the interaction between the neuron and the electric field. J Neuroeng Rehabil. 2015 Aug 12;12:65. doi: 10.1186/s12984-015-0061-1.

[13]. Liu, W.K., Li, S. & Park, H.S. Eighty Years of the Finite Element Method: Birth, Evolution, and Future. *Arch Computat Methods Eng* 29, 4431–4453 (2022). https://doi.org/10.1007/s11831-022-09740-9.

[14]. Greengard L, Rokhlin V. A fast algorithm for particle simulations. J. Comput. Phys. 1987;73(2):325-348. doi: 10.1016/0021-9991(87)90140-9.

[15]. Greengard L., Rokhlin V. A new version of the Fast Multipole Method for the Laplace equation in three dimensions. Acta Numerica, 6:229–269, 1997.

[16]. Gimbutas Z, Greengard L, Magland J, Rachh M, Rokhlin V. fmm3D Documentation. Release 0.1.0. 2019-2024. Online: https://github.com/flatironinstitute/FMM3D & https://github.com/flatironinstitute/FMM3D/blob/master/fmm3d_manual.pdf.

[17]. Greengard L, Gueyffier D, Martinsson PG, Rokhlin V (May 2009). "Fast direct solvers for integral equations in complex three-dimensional domains". Acta Numerica. 18: 243–275. doi:10.1017/S0962492906410011. ISSN 1474-0508. S2CID 58895952.

[18]. Makarov SN, Noetscher GM, Raij T, Nummenmaa A. A Quasi-Static Boundary Element Approach with Fast Multipole Acceleration for High-Resolution Bioelectromagnetic Models. IEEE Trans Biomed Eng. 2018 Mar 7. doi: 10.1109/TBME.2018.2813261.

[19]. Noetscher GM, Tang D, Nummenmaa AR, Bingham CS, McIntyre CC, Makaroff SN. Estimations of Charge Deposition onto Convoluted Axon Surfaces within Extracellular Electric Fields. IEEE Trans Biomed Eng. 2023 Aug 3; doi: 10.1109/TBME.2023.3299734.

[20]. Makaroff SN, Nummenmaa AR, Noetscher GM, Qi Z, McIntyre CC, Bingham CS. Influence of charges deposited on membranes of human hyperdirect pathway axons on depolarization during subthalamic deep brain stimulation. J Neural Eng. 2023 Jul 19;20(4). doi: 10.1088/1741-2552/ace5de.

[21]. Rattay F. Analysis of models for external stimulation of axons. IEEE Trans Biomed Eng. 1986 Oct;33(10):974-7. doi: 10.1109/TBME.1986.325670. PMID: 3770787.

[22]. Rattay F. Modeling the excitation of fibers under surface electrodes. IEEE Trans Biomed Eng. 1988 Mar;35(3):199-202. doi: 10.1109/10.1362.

[23]. Rattay F. Analysis of models for extracellular fiber stimulation. IEEE Trans Biomed Eng. 1989 Jul;36(7):676-82. doi: 10.1109/10.32099.

[24]. Markram H, Muller E, Ramaswamy S, Reimann MW, Abdellah M, Sanchez CA, Ailamaki A, Alonso-Nanclares L, Antille N, Arsever S, Kahou GA, Berger TK, Bilgili A, Buncic N, Chalimourda A, Chindemi G, Courcol JD, Delalondre F, Delattre V, Druckmann S, Dumusc R, Dynes J, Eilemann S, Gal E, Gevaert ME, Ghobril JP, Gidon A, Graham JW, Gupta A, Haenel V, Hay E, Heinis T, Hernando JB, Hines M, Kanari L, Keller D, Kenyon J, Khazen G, Kim Y, King JG, Kisvarday Z, Kumbhar P, Lasserre S, Le Bé JV, Magalhães BR, Merchán-Pérez A, Meystre J, Morrice BR, Muller J, Muñoz-Céspedes A, Muralidhar S, Muthurasa K, Nachbaur D, Newton TH, Nolte M, Ovcharenko A, Palacios J, Pastor L, Perin R, Ranjan R, Riachi I, Rodríguez JR, Riquelme JL, Rössert C, Sfyrakis K, Shi Y, Shillcock JC, Silberberg G, Silva R, Tauheed F, Telefont M, Toledo-Rodriguez M, Tränkler T, Van Geit W, Díaz JV, Walker R, Wang Y, Zaninetta SM, DeFelipe J, Hill SL, Segev I,

Schürmann F. Reconstruction and Simulation of Neocortical Microcircuitry. Cell. 2015 Oct 8;163(2):456-92. doi: 10.1016/j.cell.2015.09.029.

[25]. Hines ML, Carnevale NT. The NEURON simulation environment. Neural Comput. 1997 Aug 15;9(6):1179-209. doi: 10.1162/neco.1997.9.6.1179. PMID: 9248061.

[26]. Dorkenwald S, Turner NL, Macrina T, Lee K, Lu R, Wu J, Bodor AL, Bleckert AA, Brittain D, Kemnitz N, Silversmith WM, Ih D, Zung J, Zlateski A, Tartavull I, Yu SC, Popovych S, Wong W, Castro M, Jordan CS, Wilson AM, Froudarakis E, Buchanan J, Takeno MM, Torres R, Mahalingam G, Collman F, Schneider-Mizell CM, Bumbarger DJ, Li Y, Becker L, Suckow S, Reimer J, Tolias AS, Macarico da Costa N, Reid RC, Seung HS. Binary and analog variation of synapses between cortical pyramidal neurons. Elife. 2022 Nov 16;11:e76120. doi: 10.7554/eLife.76120.

[27]. Pilgrim C, Reisert I, Grab D. Volume densities and specific surfaces of neuronal and glial tissue elements in the rat supraoptic nucleus. J Comp Neurol. 1982 Nov 10;211(4):427-31. doi: 10.1002/cne.902110409.

[28]. Lehmenkühler A, Syková E, Svoboda J, Zilles K, Nicholson C. Extracellular space parameters in the rat neocortex and subcortical white matter during postnatal development determined by diffusion analysis. Neuroscience. 1993 Jul;55(2):339-51. doi: 10.1016/0306-4522(93)90503-8.

[29]. Mota B, Herculano-Houzel S. All brains are made of this: a fundamental building block of brain matter with matching neuronal and glial masses. Front Neuroanat. 2014 Nov 12;8:127. doi: 10.3389/fnana.2014.00127.

[30]. Krassowska W, Neu JC. Response of a single cell to an external electric field. *Biophys J.* 1994 Jun;66(6):1768-76. doi: 10.1016/S0006-3495(94)80971-3.

[31]. Pourtaheri N, Ying W, Kim JM, Henriquez CS. Thresholds for transverse stimulation: fiber bundles in a uniform field. *IEEE Trans Neural Syst Rehabil Eng*. 2009 Oct;17(5):478-86. doi: 10.1109/TNSRE.2009.2033424.

[32]. Klee M, Plonsey R. Stimulation of spheroidal cells-The role of cell shape. 1976. *IEEE Trans Biomed Eng*. Jul;23(4):347-54. PMID: 1278928.

[33]. Saad Y. Iterative Methods for Sparse Linear Systems. 2nd Ed., Society for Industrial and Applied Mathematics. 2003. ISBN 978-0-89871-534-7.

[34]. Siebner HR, Funke K, Aberra AS, Antal A, Bestmann S, Chen R, Classen J, Davare M, Di Lazzaro V, Fox PT, Hallett M, Karabanov AN, Kesselheim J, Beck MM, Koch G, Liebetanz D, Meunier S, Miniussi C, Paulus W, Peterchev AV, Popa T, Ridding MC, Thielscher A, Ziemann U, Rothwell JC, Ugawa Y. Transcranial magnetic stimulation of the brain: What is stimulated? - A consensus and critical position paper. Clin Neurophysiol. 2022 Aug;140:59-97. doi: 10.1016/j.clinph.2022.04.022.

[35]. Maccabee PJ, Amassian VE, Eberle LP, Cracco RQ. Magnetic coil stimulation of straight and bent amphibian and mammalian peripheral nerve in vitro: locus of excitation. J Physiol. 1993 Jan;460:201-19. doi: 10.1113/jphysiol.1993.sp019467. PMID: 8487192; PMCID: PMC1175209.

[36]. *MICrONS Consortium*. Online: https://www.microns-explorer.org/cortical-mm3

[37]. Jia Wan, Wanhua Li, Atmadeep Banerjee, Jason Ken Adhinarta, Evelina Sjostedt, Jingpeng Wu, Jeff Lichtman, Hanspeter Pfister, Donglai Wei. TriSAM: Tri-Plane SAM for

zero-shot cortical blood vessel segmentation in VEM images. arXiv:2401.13961v1. Jan. 2024. doi: https://doi.org/10.48550/arXiv.2401.13961.

[38]. Dorkenwald S, Turner NL, Macrina T, Lee K, Lu R, Wu J, Bodor AL, Bleckert AA, Brittain D, Kemnitz N, Silversmith WM, Ih D, Zung J, Zlateski A, Tartavull I, Yu SC, Popovych S, Wong W, Castro M, Jordan CS, Wilson AM, Froudarakis E, Buchanan J, Takeno MM, Torres R, Mahalingam G, Collman F, Schneider-Mizell CM, Bumbarger DJ, Li Y, Becker L, Suckow S, Reimer J, Tolias AS, Macarico da Costa N, Reid RC, Seung HS. Binary and analog variation of synapses between cortical pyramidal neurons. Elife. 2022 Nov 16;11:e76120. doi: 10.7554/eLife.76120.

[39]. Fellner A, Heshmat A, Werginz P, Rattay F. A finite element method framework to model extracellular neural stimulation. J Neural Eng. 2022 Apr 7;19(2). doi: 10.1088/1741-2552/ac6060.

[40]. Czerwonky DM, Aberra AS, Gomez LJ. (2023-12-16), "A Boundary Element Method of Bidomain Modeling for Predicting Cellular Responses to Electromagnetic Fields", BioRxiv: The Preprint Server for Biology, doi:10.1101/2023.12.15.571917.

Supplement to the manuscript:
Electromagnetic Modeling within a Microscopically Realistic Brain – Implications for Brain Stimulation

Contents

A. Post-processing segmentation and skeletonization of L2/L3 sample

A1. Preparing neuronal surface meshes for electromagnetic modeling

A2. Estimating volumetric density of neuronal cells from surface meshes and comparing it with the known values

A3. Healing and refining centerlines of neuronal processes – neuron skeletons

A4. Estimating sample anisotropy from neuron morphology

A5. Selecting proper neurons with the longest retained axonal arbors for biophysical modeling

A6. Summary of post-processing parameters

B. Membrane mesh intersection maps and intersection resolution method

B1. Mesh intersection maps

B2. Test of intersection resolution method

C. Biophysical modeling

C1. Summary of NEURON modeling parameters

C2. Pulse forms of the stimulation field

C3. Reduction of neuronal activating thresholds for different pulse forms and myelinated axons

D. Estimates of absolute TMS activating threshold of mouse primary motor cortex from experimental data

D1. Experimental procedure

D2. Modeling setup

D3. Estimating electric field strength within mouse brain from measured motor evoked potentials

D4. Comparison with previously reported computed data for mouse primary motor cortex

Supplement A. Post-processing segmentation and skeletonization of L2/L3 sample

A1. Preparing neuronal surface meshes for electromagnetic modeling

All 396 neurons were initially numbered following the y-coordinate (dorsal-to-ventral direction) of their center of mass. The lowest numbers correspond to the deepest neurons where the bulk of the axonal arbor was cut out (see below). Neurons with the highest numbers have the (relatively) well developed axonal arbor (Fig. 1f,g of the main text).

Initial computational surface triangular meshes for the neurons downloaded from the MICrONS database [1] were not entirely suitable for accurate numerical analysis. Automated CGAL alpha wrapping C++ library [2],[3] was used for all neurons to re-mesh the data and convert them to the strictly 2 manifold high-quality (min triangle quality is 0.1) high-resolution individual surface objects. A relative α (vs 1e-3*longest diagonal; parameter α limits the maximum triangle size) of 1000 and a relative offset (vs 1e-3*longest diagonal, parameter offset limits the tightness of the result around the input mesh) of 4000 were used in the CGAL program. We were unable to properly heal 13 cells. These cells were eliminated from the analysis which reduced the total cell number from 396 to 383.

Fig. 2a of the main text illustrates the final membrane mesh for neuron #238. A typical membrane mesh has approximately 1-2 million triangles on average, with an average facet size of 100 nm. This is necessary to keep a proper spatial accuracy for intersection resolution (Section 2.3 of the main text) and also resolve microscopic, localized variations of the impressed electric field. The total number of facets of the sample approaches 0.5 billion. The average facet size is 100 nm. An identical procedure also was applied to the microcapillaries (cf. Fig. 1d of the main text).

A2. Estimating volumetric density of neuronal cells from surface meshes and comparing it with the known values

The volumetric fraction of all neuronal cells within the SEM (scanning electron microscopy) volume was estimated as 30%±5% by computing the volume of each neuron using the CGAL tools and also taking into account neuronal mesh intersections (section 2.3 of the main text).

This is less than the known estimates in rats and mice [4],[5],[6] because all neurons with somas outside the brain sample were omitted and their dendritic/axonal processes, which are still within the sample, were ignored.

In general, the brain tissue is composed of extracellular space and intracellular space, i.e. neurons and glia cells (intracellular space) do not take up all the volume of brain tissue. Oxygen molecules and nutrients (e.g. glucose molecules) diffuse from capillary through extracellular space to neurons and glia, and are taken up through transporters. According to [4] (rats), neuronal elements occupy about 74% and glial elements about 8% of the total volume. According to [5] (rats), the extracellular space takes up about 20% of total cortex volume in adult rats. According to [6] (Table 5), the fraction of neuronal mass in mice cerebral cortex is 70%.

Based on these data and also on some data from Ref. [7], we estimate the realistic volume fraction of neuronal mass in mice neocortex as approximately 70%.

A3. Healing and refining centerlines of neuronal processes – neuron skeletons

The original neuronal skeletons or morphological reconstructions (301 in total) from the MICrONS database [1] didn't remain entirely in the center of the corresponding neuronal processes represented by the relevant surface mesh. They also had a rather sparse discretization. The skeleton branches or centerlines have been therefore refined, smoothed, and corrected via an automated in-house routine that finds every point's distance from the enclosing membrane walls in the up, down, left, right, in, and out directions and averages them for every cross-section of the relevant triangular mesh. Fig. 2b,c of the main text shows the centerlines of the neuronal processes healed in such a way. We attempted to maintain a nearly uniform spatial resolution of 100 nm for the centerline discretization(observation) points, which should be sufficient for catching up fast field variations over the length on the order of 1 μm or so. We were unable to properly heal 34 centerlines. These centerlines were eliminated from the subsequent analysis which reduced their total number from 301 to 267.

We also estimated the average axonal length per neuron, with the maximum length of 8.3 mm for inhibitory neuron #191 and the minimum length of 0 mm (for 39 other neurons in total).

A4. Estimating sample anisotropy from neuron morphology

To estimate the degree of anisotropy, we introduced an equivalent straight–fiber density measure. It is obtained when centerlines for all neuronal processes including both axons and dendrites are projected onto three Cartesian axes (Fig. S1b,c,d below). This density was estimated by finding the total projection length and then dividing this value by the product of three sample dimensions (the sample volume). The following values of the equivalent straight fiber density have been obtained: $1.3e5\ \mathrm{mm}^{-2}$ for the medial-lateral or x direction, $1.0e5\ \mathrm{mm}^{-2}$ for the dorsal-ventral or y direction and $0.9e5\ \mathrm{mm}^{-2}$ for the anterior-posterior or z direction.

A5. Selecting proper neurons with the longest retained axonal arbors for biophysical modeling

The lengths of all segments of the neuronal processes (axons and dendrites) were computed using the available `*.swc` files from the MICrONS database. Fig. S1a shows the length of axonal arbor per neuron, now sorted in descending order. It is seen that neurons with numbers greater than 90-100 have a vanishingly short axonal arbor, which was cut out of this sample almost entirely. Therefore, they were eliminated from the final results of biophysical analysis (otherwise non-physical, large values of the activating threshold could be obtained) but were still kept for the electromagnetic analysis.

Thus, only the neurons with the overall axonal length of 0.5 mm or greater (with the sorted numbers from 1 to 90, Fig. S1a below) were included into the relevant biophysical modeling outcomes – see Fig. 6 of the main text, Figs. S4 through S7 of Supplement C, and also Tables 1 and 2 of the main text.

Fig. S1b additionally shows the total length of axonal arbor per neuron projected onto three Cartesian axes (x, y, z). The neurons have been sorted as in Fig. S1a). Similarly, Fig. S1c demonstrates projected (onto three Cartesian axes) length of dendritic arbor per neuron. The neurons have again been sorted as in Fig. S1a. Finally, Fig. S1d demonstrates the projected length of all neuronal processes (axonal plus dendritic) per neuron. The neurons have been sorted as in Fig. S1a. Again, one clearly observes in Fig. S1b that the neurons with numbers greater than approximately 90 have vanishingly small axonal arbor, which was cut out of the brain sample almost entirely.

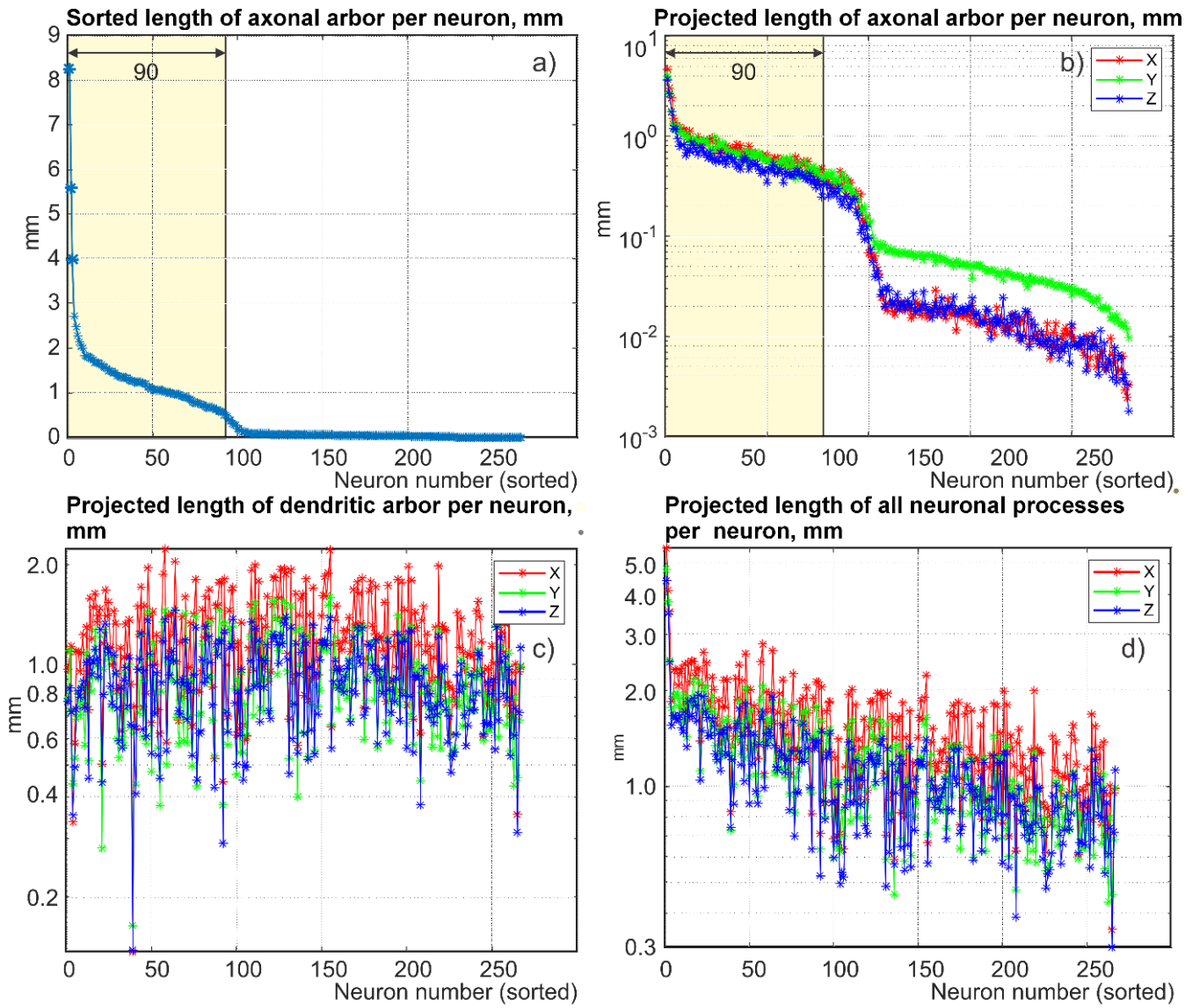

Fig. S1. a) Sorted (in descending order) length of axonal arbor per neuron. Neurons with numbers greater than approximately 90 have vanishingly small axonal arbor, which was cut out of the sample almost entirely. b) Projected (onto three Cartesian axes) length of axonal arbor per neuron. The neurons have been sorted as in a). c) Projected (onto three Cartesian axes) length of dendritic arbor per neuron. The neurons have been sorted as in a). c,d) Projected (onto three Cartesian axes) length of all neuronal processes (axonal plus dendritic) for all neurons with the healed morphological reconstructions. The neurons have been sorted as in a).

A6. Summary of post-processing parameters

Table S1 of this Supplement lists major topological and biophysical parameters of the created computational testbed (electromagnetic and biophysical) including estimated sample anisotropy. Emphasize again that both the facet size for membrane discretization and the skeleton's spatial resolution for the biophysical analysis were kept at approximately 100 nm to resolve large yet very localized variations of the impressed field due to multiple nearfield interactions of the neuronal processes as well as to resolve multiple intersections of neuronal arbors of different neurons (Fig. 2 of the main text).

Table S1. Post-procesing parameters of the L2/L3 mouse brain sample.383 Neurons were kept for electromagnetic analysis. Data for 90 neurons with the longest axonal arbor were included in the final biophysical outcomes.

Parameter	Value
Neuronal meshes for EM modeling	396 – initial; 383 – final
Vascular meshes for EM modeling	34, partially disconnected
Total mesh size/triangular facet size/triangular facet quality	~0.5 billion facets/100 nm/0.1 min
Volumetric fraction of neuronal mass within the sample	~30±5%
Neuron skeletons	301 initial/267 final
Spatial discretization of healed skeletons	100 nm
Largest length of axonal arbor per neuron	8.3 mm for inhibitory neuron #191 and 2.3 mm for excitatory neuron #333
Equivalent straight-fiber density of neuronal processes in three orthogonal directions (sample anisotropy)	Fiber density of $1.3e5\ \mathrm{mm}^{-2}$ for the medial-lateral or x direction, $1.0e5\ \mathrm{mm}^{-2}$ for the dorsal-ventral or y direction and $0.9e5\ \mathrm{mm}^{-2}$ for the anterior-posterior or z direction
Neuron skeletons with developed axonal arbor suitable for biophysical modeling	90

Supplement B. Membrane mesh intersection maps

B1. Mesh intersection maps

Fig. S2a demonstrates a typical surface mesh intersection map. Two neighboring excitatory neurons – #238 and #290 – have been chosen.

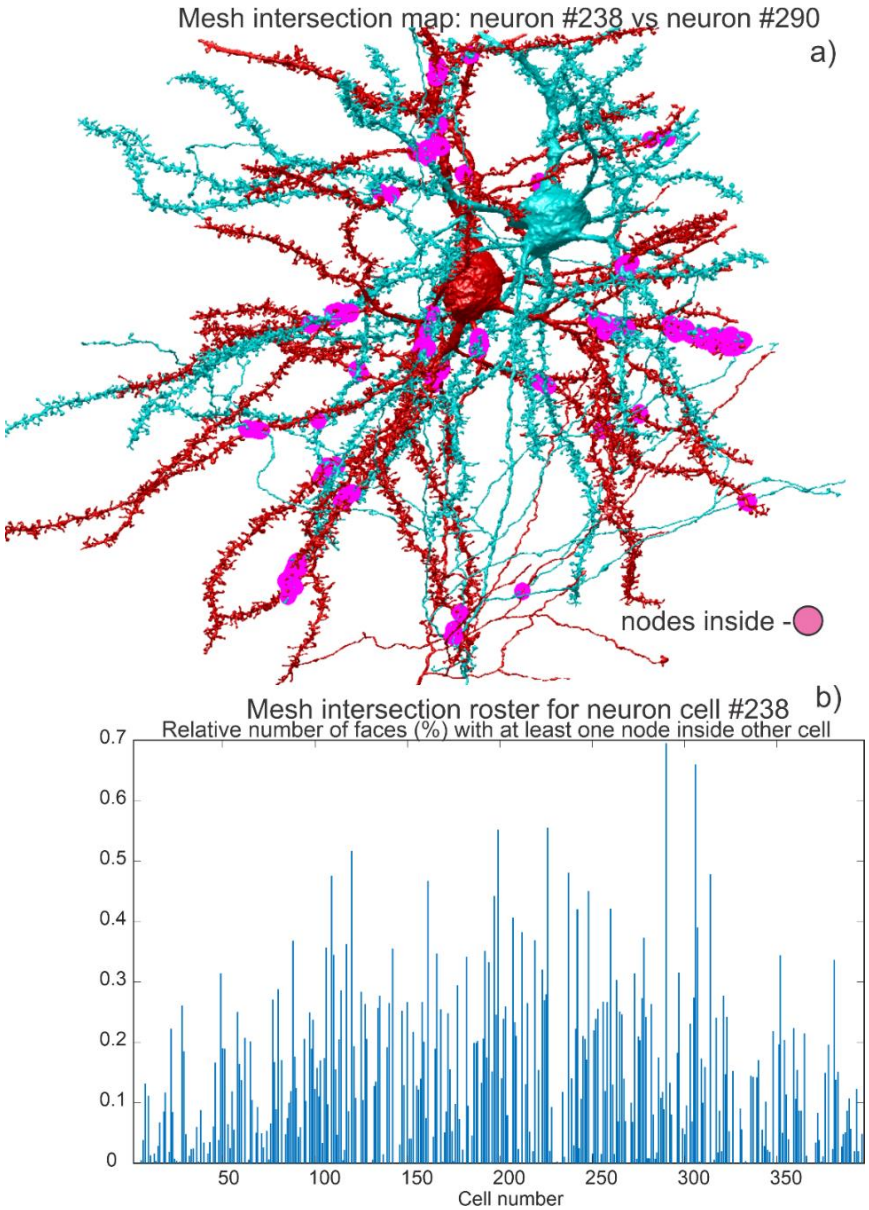

Fig. S2. a) Surface mesh intersection map between neighboring excitatory neurons #238 and #290, respectively. Intersection domains are marked by magenta color. b) Mesh intersection roster of neuron #238 with all other neurons of the sample. The y axis gives the relative number of facets (% versus the total number of faces for neuron #238) with at least one facet node contained within another neuronal shell. The x axis is the neuron number.

In Fig. S2a, the mesh intersection domains are marked by magenta color. There are approximately 30 such independent intersection domains.

Fig. S2b also presents a mesh intersection roster of excitatory neuron #238 with all other neurons of the sample. It is observed in Fig. S2b that neuron #238 intersects with almost all neurons of the sample. Similar, and even more dramatic results were observed for other larger neurons of the sample. To identify the mesh intersections for large yet manifold meshes, we used vectorized function `inpolyhedron` written by Sven Holcombe in MATLAB [8]. Still, this has been a very time-consuming operation.

B2. Test of intersection resolution method

The intersection resolution method described in Section 2.3 was tested as follows. We selected a smaller set of 22 neurons (set #1). We further refined all surface meshes of this set in proportion 1:4. This comprises set #2. We analyzed set#1 and computed collinear electric fields at the skeleton centerlines. The same operation was done with set #2. We computed the average normalized 2-norm difference between two sets of projected fields and found that this error is within 6%.

Supplement C. Biophysical modeling

C1. Summary of NEURON modeling parameters

Standard NEURON software [9] has been used to study neural activation in response to the impressed extracellular potential/electric field computed previously at the centerlines of the neuronal processes. The post-processed neuron morphology (described in Supplement A) for 267 available neuron models (in `swc` format, including soma, axons, apical and basal dendrites) was loaded into NEURON by its `Import3D` tool. Following references [10],[11],[12] we applied the existing ion channel models for rodents (rats) which have been used starting with Aberra et al. [10]. We used 6 active channels for the soma, 8 active channels for the axons, 1 active channel for the basal dendrites, and 3 active channels for the apical dendrites. The implementation for the most important axonal channels was tested and verified against in-house MATLAB-based software.

The centerlines of the neuronal processes were discretized in space with the step $d_\lambda = L/\left[n_{seg}\lambda_w(f = 100\ Hz)\right]$, where L is the section length, n_{seg} is the number of segments in this section, and $\lambda_w = \sqrt{D/(4\pi f R_a c_m)}$ is the length constant, with D being the neuron diameter; f is a frequency that is high enough for transmembrane current to be primarily capacitive, but is still within the frequency range relevant to neuronal function. Here, R_a is the resistivity of axoplasm and c_m is the membrane capacity per unit area. In the computations, we tested several d_λ values between $d_\lambda = 0.01$ and $d_\lambda = 0.0005$, respectively, to address expected rapid field variations at microscale. We compared the results for a representative number (6 in total) of large neurons with many local extracellular field variations. The difference in the activating thresholds was found to be negligibly small between the two extreme values. Therefore, the value $d_\lambda = 0.01$ or 0.005 has been routinely used everywhere after test runs. The time step size was chosen as $1\ \mu s$.

C2. Pulse forms of the stimulation field

As the simple base form, we used the monophasic rectangular pulse form for the primary or impressed field starting at $t = 0$ and with a duration of $0.1\ \mathrm{ms}$ – cf. Fig. S3a,b). The positive and negative pulses (positive and negative electric field directions) have been modeled separately. Along with this, we used a realistic biphasic TMS (transcranial magnetic stimulation) pulse form (Fig. S3c) from a B65 coil of MagVenture, Denmark measured in the Noninvasive Neuromodulation Unit, Experimental Therapeutics & Pathophysiology Branch, NIMH. Both positive and negative pulse forms have been investigated. Some computations have also been done for a monophasic TMS pulse.

The pulse magnitude was gradually increased until the neuron activating criterion (the transmembrane voltage goes above zero anywhere in the arbor [10]) was met. After that, the amplitude was decreased with a smaller step to pass the activating threshold in the opposite direction. This automated search procedure – the bisection method – requires approximately 15 steps and about 15-25 min per neuron on average. The total simulation time for all neurons with x, y, and z polarizations for both primary and total extracellular fields/potentials did not exceed one week per polarization.

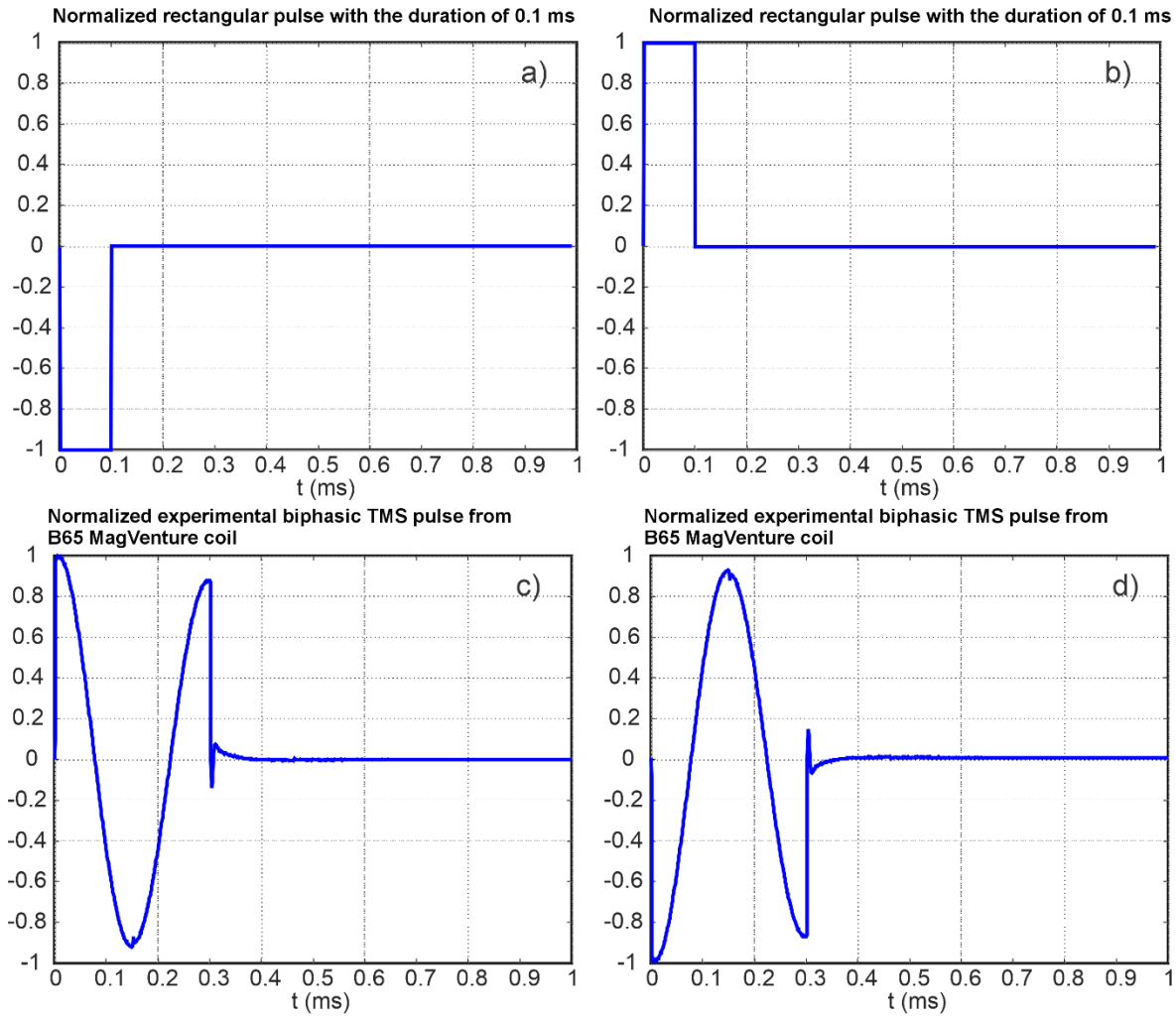

Fig. S3. Four pulse forms for the primary impressed field used for biophysical modeling.

C3. Reduction of neuronal activating thresholds for different pulse forms and myelinated axons

Figs. S4 through S7 given below replicate Fig. 6 of the main text for different pulse forms and with considering axonal myelination. They have been used to fill out Table 2 of the main text.

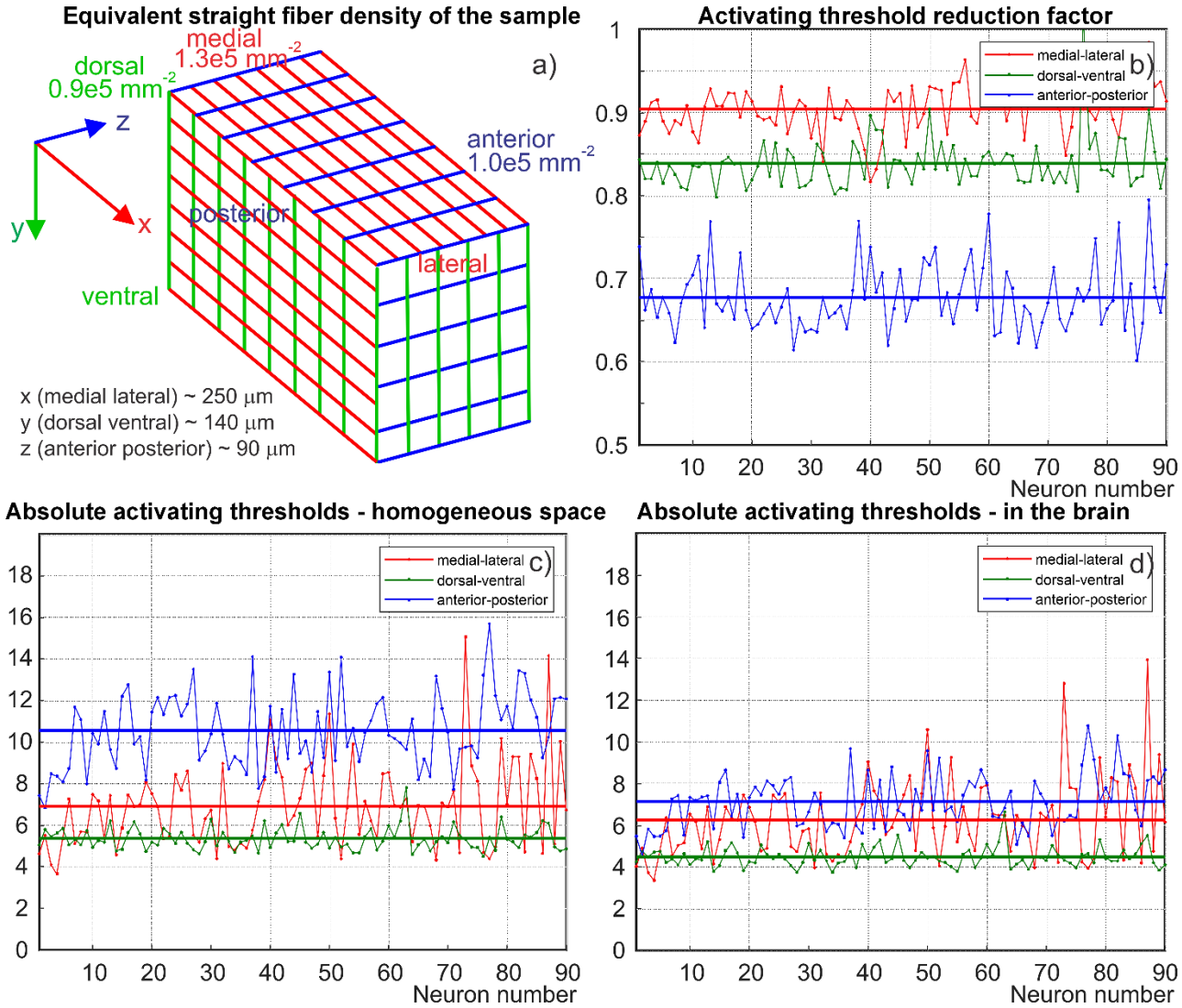

Fig. S4. a) Equivalent straight fiber density distribution of the sample characterizing its anisotropy. b) Activating threshold reduction factor for the first 90 neurons with the longest axonal arbor (sorted) for three polarizations of the primary electric field: medial-lateral (red), dorsal-ventral (green), and anterior-posterior (blue). c) Absolute activating thresholds for the same 90 neurons in homogeneous space. d) Absolute activating thresholds for the same 90 neurons within the sample. The units in c,d) are given in terms of the base field strength of 100 V/m; one unit corresponds to 100 V/m. These results are given for the case of the unmyelinated axonal arbor and a positive rectangular activation monophasic pulse with the duration of 0.1 ms.

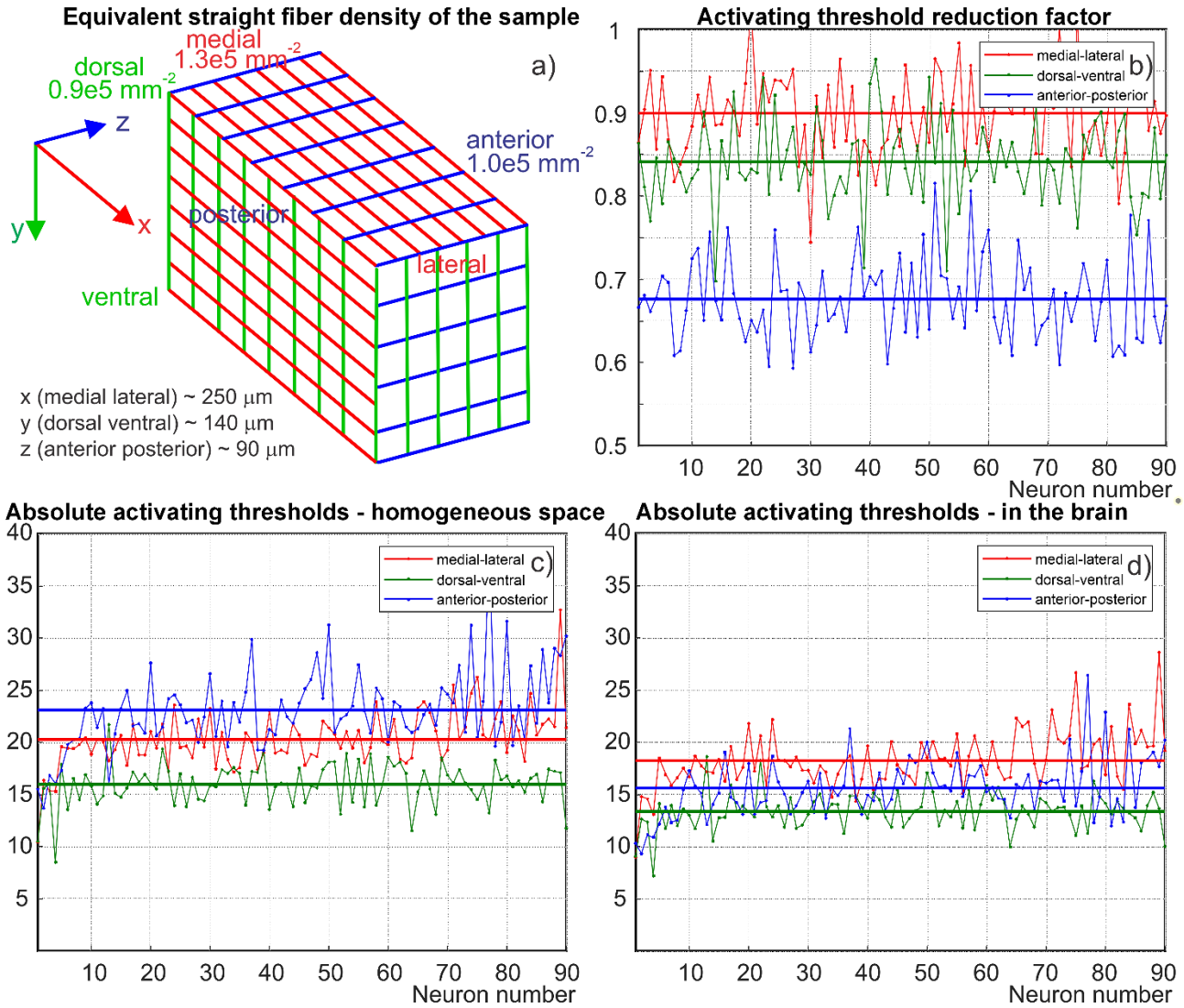

Fig. S5. a) Equivalent straight fiber density distribution of the sample characterizing its anisotropy. b) Activating threshold reduction factor for the first 90 neurons with the longest axonal arbor (sorted) for three polarizations of the primary electric field: medial-lateral (red), dorsal-ventral (green), and anterior-posterior (blue). c) Absolute activating thresholds for the same 90 neurons in homogeneous space. d) Absolute activating thresholds for the same 90 neurons within the sample. The units in c,d) are given in terms of the base field strength of 100 V/m; one unit corresponds to 100 V/m. These results are given for the case of the unmyelinated axonal arbor and a negative biphasic activation pulse with the duration of 0.3 ms (Fig. S3).

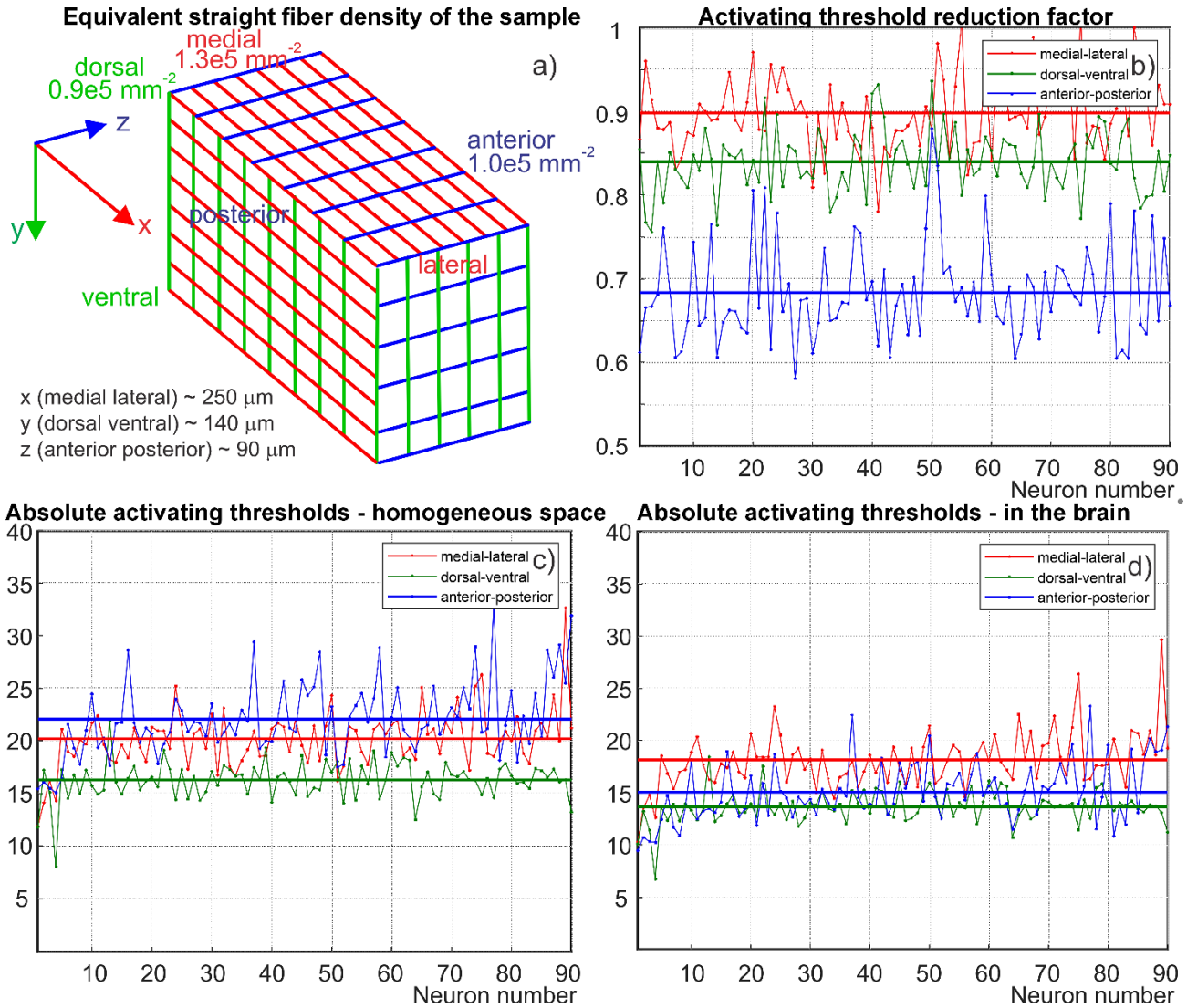

Fig. S6. a) Equivalent straight fiber density distribution of the sample characterizing its anisotropy. b) Activating threshold reduction factor for the first 90 neurons with the longest axonal arbor (sorted) for three polarizations of the primary electric field: medial-lateral (red), dorsal-ventral (green), and anterior-posterior (blue). c) Absolute activating thresholds for the same 90 neurons in homogeneous space. d) Absolute activating thresholds for the same 90 neurons within the sample. The units in c,d) are given in terms of the base field strength of 100 V/m; one unit corresponds to 100 V/m. These results are given for the case of the unmyelinated axonal arbor and a negative biphasic activation pulse with the duration of 0.3 ms (Fig. S3).

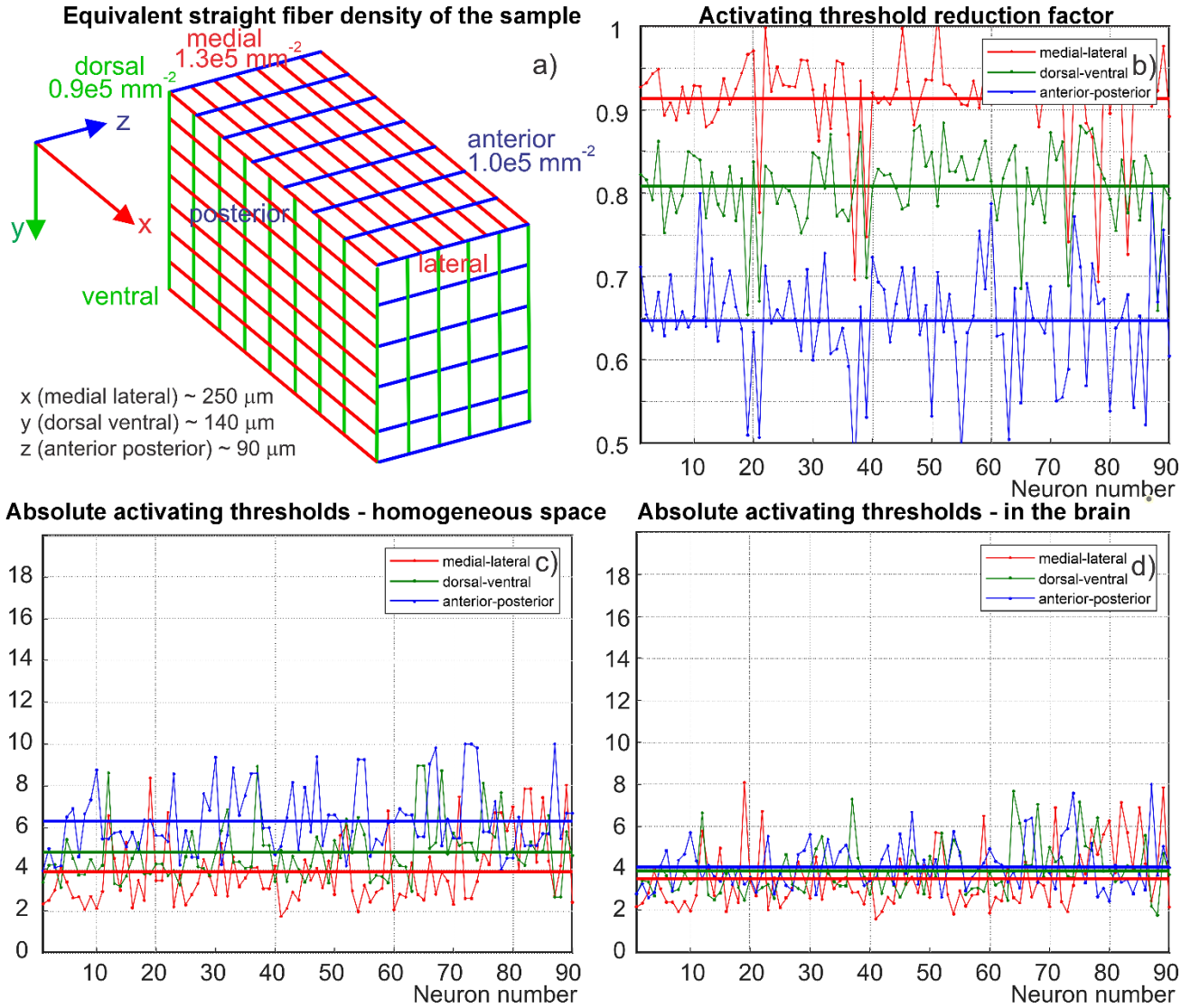

Fig. S7. a) Equivalent straight fiber density distribution of the sample characterizing its anisotropy. b) Activating threshold reduction factor for the first 90 neurons with the longest axonal arbor (sorted) for three polarizations of the primary electric field: medial-lateral (red), dorsal-ventral (green), and anterior-posterior (blue). c) Absolute activating thresholds for the same 90 neurons in homogeneous space. d) Absolute activating thresholds for the same 90 neurons within the sample. The units in c,d) are given in terms of the base field strength of 100 V/m; one unit corresponds to 100 V/m. These results are given for the case of the myelinated axonal arbor and a negative rectangular activation monophasic pulse with the duration of 0.1 ms.

Supplement D. Estimates of absolute TMS activating threshold of mouse primary motor cortex from experimental data

D1. Experimental procedure

In vivo, TMS experiments were performed on male C57BL/6J mice (n¼6) using a custom rodent TMS coil with a magnetic core (Fig. S8c). Animals were anesthetized with sodium pentobarbital intraperitoneally (50 mg/kg), MEP (motor evoked potential) was recorded using a similar approach reported by Rotenberg et al. [13]. All procedures were approved by National Institute on Drug Abuse/NIH (NIDA) animal care and use committee. The coil was mounted to a customized three-axis micromanipulator.

The focal electrical field point was carefully aligned to the targeted mouse motor cortex. Fine adjustments of the coil were made to induce limb twitch on the contralateral hindlimb, but not the ipsilateral hindlimb, any of the forelimbs or any other body part. More detailed description of TMS experiments is given in [14]. Detailed description of a similar custom focal TMS rodent coil was previously given in Ref. [15].

D2. Modeling setup

Detailed brain model [16] (Fig. S8a) along with the model of the custom TMS rodent coil with a magnetic core (Fig. S8c) has been used to simulate the electric field distribution both in three principal planes (Fig. S8b) as well as just inside the brain compartments (Fig S8d). The skin shell conductivity was chosen as 0.3 S/m, the skull conductivity – 0.01 S/m. All brain compartments were assigned the conductivity of 0.3 S/m. Some conductivity variations were studied. They did not substantially alter the computational results. In general, the small mouse body quite significantly (by a factor of ~2 or so) blocks the primary applied solenoidal electric field of the TMS coil.

D3. Estimating electric field strength within mouse brain from measured motor evoked potentials

Simulations were performed for two experimental parameters – the coil current of ~3,000 A and dI/dt of 94 A/μs – corresponding to the induced MEPs. Fig. S8d shows the resulting magnitude of the total electric field just inside the brain compartments. The circle approximately labels the area of the primary motor cortex. One observes that the field strength there approaches 90 V/m. Conductivity variations of the head compartments lead to the field strength changes within the M1 area (white circle in Fig. S8) to within ±15% about this value. Similar results have been obtained

for the total field magnitude distributions in three principal planes shown in Fig. S8e. Another mouse CAD model [17] has also been tested; it also generated very similar results.

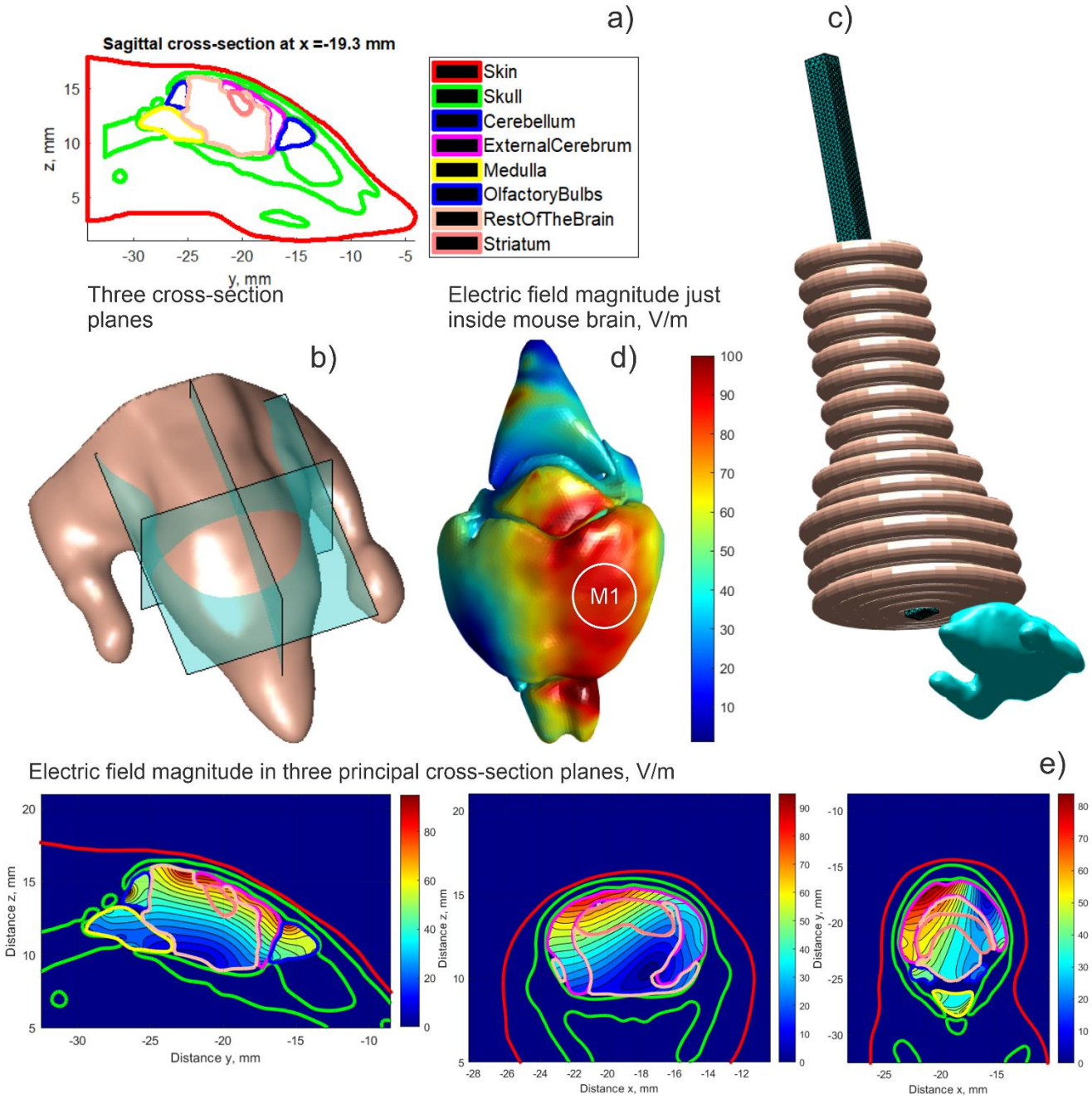

Fig. S8. a) CAD Mouse model [16]. b) Three principal planes for field output. c) Shape and positioning the custom TMS coil. d) Electric field magnitude distribution just inside mouse brain. Circle approximately indicates the primary motor cortex.

D4. Comparison with previously reported computed data for mouse primary motor cortex

In Ref. [17], the maximum fields strengths of 81.3 V/m,113.4 V/m, and 86.5 V/m in the brain have been computed for three different coil positions of a 25 mm figure-8 coil for the coil's dI/dt of 100 A/μs In Ref. [18], it was concluded from numerical experiments that, for 100 A/μs, the predicted fields in mouse brain are on the order of 120 V/m.

Our experimental data agree with these modeling predictions. They suggest that 90 V/m ± 15% is a reasonable MEP estimate in a mouse brain.

References – Supplements A, B, C, D

[1]. [MICrONs Consortium et al. Functional connectomics spanning multiple areas of mouse visual cortex. bioRxiv originally published 2021.07.28.454025/updated 2023.04.19; doi: https://www.biorxiv.org/content/10.1101/2021.07.28.454025v3 . Online: https://www.microns-explorer.org/phase1. Release Notes (v185).

[2]. CGAL online: https://github.com/CGAL/cgal

[3]. Pierre Alliez and David Cohen-Steiner and Michael Hemmer and Cédric Portaneri and Mael Rouxel-Labbé. 3D Alpha Wrapping. In CGAL User and Reference Manual. CGAL Editorial Board, 5.6 edition, 2023.

[4]. Pilgrim C, Reisert I, Grab D. Volume densities and specific surfaces of neuronal and glial tissue elements in the rat supraoptic nucleus. J Comp Neurol. 1982 Nov 10;211(4):427-31. doi: 10.1002/cne.902110409.

[5]. Lehmenkühler A, Syková E, Svoboda J, Zilles K, Nicholson C. Extracellular space parameters in the rat neocortex and subcortical white matter during postnatal development determined by diffusion analysis. Neuroscience. 1993 Jul;55(2):339-51. doi: 10.1016/0306-4522(93)90503-8.

[6]. Mota B, Herculano-Houzel S. All brains are made of this: a fundamental building block of brain matter with matching neuronal and glial masses. Front Neuroanat. 2014 Nov 12;8:127. doi: 10.3389/fnana.2014.00127.

[7]. Keller D, Erö C, Markram H. Cell Densities in the Mouse Brain: A Systematic Review. Front Neuroanat. 2018 Oct 23;12:83. doi: 10.3389/fnana.2018.00083.

[8]. Sven Holcombe (2024). inpolyhedron - are points inside a triangulated volume? (https://www.mathworks.com/matlabcentral/fileexchange/37856-inpolyhedron-are-points-inside-a-triangulated-volume), MATLAB Central File Exchange. Retrieved February 5, 2024.

[9]. Hines ML, Carnevale NT. The NEURON simulation environment. Neural Comput. 1997 Aug 15;9(6):1179-209. doi: 10.1162/neco.1997.9.6.1179. PMID: 9248061.

[10]. Aberra AS, Peterchev AV, Grill WM. Biophysically realistic neuron models for simulation of cortical stimulation. J Neural Eng. 2018 Dec;15(6):066023. doi: 10.1088/1741-2552/aadbb1.

[11]. Aberra AS, Wang B, Grill WM, Peterchev AV. Simulation of transcranial magnetic stimulation in head model with morphologically-realistic cortical neurons. Brain Stimul. 2020 Jan-Feb;13(1):175-189. doi: 10.1016/j.brs.2019.10.002.

[12]. Weise K, Worbs T, Kalloch B, Souza VH, Jaquier AT, Van Geit W, Thielscher A, Knösche TR. Directional Sensitivity of Cortical Neurons Towards TMS Induced Electric Fields bioRxiv 2023.07.06.547913; doi: https://doi.org/10.1101/2023.07.06.547913.

[13]. Rotenberg A, Muller PA, Vahabzadeh-Hagh AM, Navarro X, López-Vales R, Pascual-Leone A, Jensen F. Lateralization of forelimb motor evoked potentials by transcranial magnetic stimulation in rats. Clin Neurophysiol. 2010 Jan;121(1):104-8. doi: 10.1016/j.clinph.2009.09.008. Epub 2009 Nov 8. PMID: 19900839; PMCID: PMC2818443.

[14]. Meng Q, Jing L, Badjo JP, Du X, Hong E, Yang Y, Lu H, Choa FS. A novel transcranial magnetic stimulator for focal stimulation of rodent brain. Brain Stimul. 2018 May-Jun;11(3):663-665. doi: 10.1016/j.brs.2018.02.018.

[15]. Makaroff SN, Nguyen H, Meng Q, Lu H, Nummenmaa AR, Deng ZD. Modeling transcranial magnetic stimulation coil with magnetic cores. J Neural Eng. 2023 Jan 25;20(1):016028. doi: 10.1088/1741-2552/acae0d. PMID: 36548994; PMCID: PMC10481791.

[16]. Serano P, Makaroff S, Ackerman JL, Nummenmaa A, Noetscher GM. Detailed high quality surface-based mouse CAD model suitable for electromagnetic simulations. Biomed Phys Eng Express. 2023 Nov 30;10(1):10.1088/2057-1976/ad0e14. doi: 10.1088/2057-1976/ad0e14.

[17]. Alekseichuk I, Mantell K, Shirinpour S, Opitz A. Comparative modeling of transcranial magnetic and electric stimulation in mouse, monkey, and human. Neuroimage. 2019 Jul 1;194:136-148. doi: 10.1016/j.neuroimage.2019.03.044.

[18]. Koponen LM, Stenroos M, Nieminen JO, Jokivarsi K, Gröhn O, Ilmoniemi RJ. Individual head models for estimating the TMS-induced electric field in rat brain. Sci Rep. 2020 Oct 15;10(1):17397. doi: 10.1038/s41598-020-74431-z.